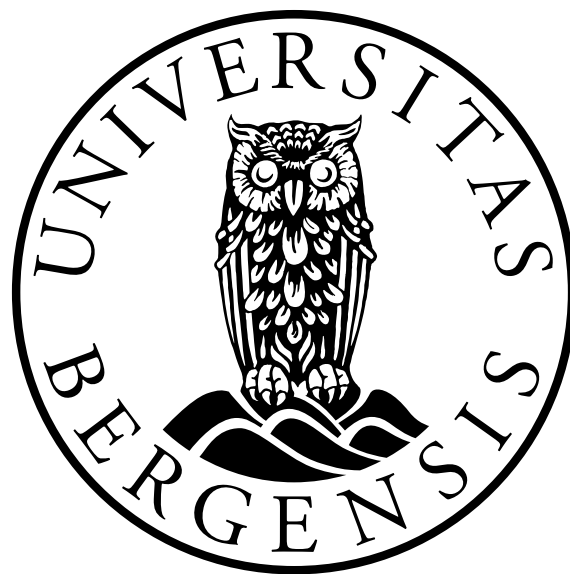


A Numerical Study of Exercise Induced Laryngeal Obstruction using Fluid-Structure Interaction

Maren Roll Lied
University of Bergen, Department of Physics and Technology
Bergen, Norway

June 1, 2017



A thesis in partial fulfilment of the requirements for the degree of *Master of Science* in the subject of Process Technology: Multiphase Systems

Acknowledgement

First and foremost I would like to thank my supervisor Prof. Pawel Kosinski for his positive attitude toward my untraditional choice of topic for my thesis. Additionally, he has an admirable devotion to his students in his genuinely positive and uplifting behaviour. I appreciate how he always makes me feel welcome at his office, no matter what I want to ask or discuss. I am very grateful for what I have learned throughout the year, and that I got the opportunity to write this thesis under his supervision.

I would like to express my appreciation to my co-supervisor Dr. Boris Balakin from the Western Norway University of Applied Sciences for being curious, critical and most of all helpful. I appreciate the discussions about physical theory and properties within the throat throughout the year. Most importantly, his knowledge within the CFD software STAR-CCM+ has been priceless when difficulties within the program has encountered.

I would also like to thank Prof. Thomas Halvorsen at Haukeland University Hospital for introducing this topic for me. Furthermore, I want to thank Dr. Ola Drange Røksund at Haukeland University Hospital for the possibility to join a test at the laboratory to see how the issue affects individuals in practice. I also want to express my appreciation to Dr. Alexander Lundervold at Western Norway University of Applied Sciences for great theoretical discussions, and his assistance when it comes to CFD modelling within this topic. In addition, I want to thank Phd. stud. Zoe Fretheim-Kelly at NMBU (Norwegian University of Life Sciences) for providing valuable data from similar conditions for horses.

Finally, I want to thank my fellow students that I have shared office with the last two years. Everything feels better when we are in it together, and I am very thankful for sharing ups and downs with you.

Last but not least I want to express my deepest appreciation to my family and friends for the support during my study time.

Bergen, June 2017

Maren Roll Lied

Abstract

During inhalation, the pressure in the lungs decreases relative to the atmospheric air pressure, so that the atmospheric air is sucked into the lungs. During strenuous exercise, exposed individuals may experience that the epiglottic folds collapse due to the ventilation-induced inspirational pressure difference. Consequently, a partially blockage of the narrowest part in the respiratory tract, i.e. in the larynx, occurs. Hence, less air reaches the lungs and breathing gets harder.

The above-described phenomenon is known as exercise induced laryngeal obstruction (EILO). As it is not well explored, numerous questions related to diagnosis and treatment still remains to be examined. A better knowledge of physical parameters being critical for individuals experiencing EILO is of particular interest. Hence, a better understanding of why some individuals are affected while others are not, is desirable.

This thesis is based on results from a previous master's thesis with the aim of taking the work a step further. By using the commercial computational fluid dynamics software STAR-CCM+, the fluid-structure interaction method was implemented to a simplified geometrical 3D-model to balance the fluid forces and the elastic forces interacting in the breathing process. The constant lung suction pressure explained above acts as the driver of the air flow.

Various values for Young's modulus were assigned to the epiglottic fold, acting as the main obstacle causing the situation arising in the larynx during EILO. Investigation of how different values for Young's modulus of the epiglottic fold affect the displacement of the fold, the volume flow at the outlet, i.e. the lungs, and the maximum velocity in the larynx were carried out.

The results of the numerical simulations with fluid-structure interaction show a decrease in the volume flow at the outlet as the displacement of the epiglottic fold increases (Young's modulus decreases), as expected. In fact, a reduction equal to 34 % is suggested as difference in volume flow reaching the lungs when comparing an EILO larynx with a normal larynx. Furthermore, the steady maximum velocity in the larynx was reduced with increasing displacement of the epiglottic fold in simulations where the pressure drop controls the flow. Based on the steady-state velocity data, individuals having Young's modulus of the epiglottic fold lower than 0.8 MPa were suggested to qualify as EILO patients. Fatigue of the epiglottic fold was suggested as a possible cause of the situation, but such a proposal needs further investigation.

Contents

1	Introduction	1
1.1	Background	1
1.2	Motivation	2
1.3	Objective	3
2	Short description of medical background	4
2.1	Basics of the laryngeal structure	4
2.2	Exercise induced obstruction	5
2.3	Exercise induced laryngeal obstruction	6
2.4	Air flow dynamics and resistance	9
3	Literature study	10
3.1	Experimental studies	10
3.2	Numerical studies	11
3.3	Combined studies	15
4	Basic computational fluid dynamics	17
4.1	Continuity equation	17
4.2	Momentum equation	18
4.3	Energy equation	20
4.4	Wall boundary conditions	20
4.5	Discretization	21
4.6	Mesh	23
5	Additional models applied	25
5.1	Turbulence models	25
5.1.1	The SST κ - ω turbulence model	25
5.2	Fluid-Structure Interaction	27
5.2.1	Structural mechanics	28
5.2.2	Fluid mechanics	29
5.2.3	Coupling of fluid and structure	30
5.2.4	Classifications of fluid-structure interactions	30
5.3	Elasticity and Young's modulus	31
6	Methodology	32
6.1	Development of model geometries	32
6.2	Preliminary analysis	37
6.2.1	Model 2 - fluid-structure interaction	38
6.2.2	Model 3 - real geometry	38
6.2.3	Calculation of the required number of steps	39

6.3	Pressure drop	39
6.4	Description of mesh	40
6.4.1	Model 1 - validation	41
6.4.2	Model 2 - fluid-structure interaction	42
6.4.3	Model 3 - real geometry	43
6.5	Selected simulation models	45
6.5.1	Fluid	45
6.5.2	Solid	47
6.6	Solvers	48
6.7	Additional essential parameters	49
6.8	Applied boundary conditions	50
6.8.1	Model 1 - validation	51
6.8.2	Model 2 - fluid-structure interaction	52
6.8.3	Model 3 - real geometry	52
6.9	Mesh morphing	53
7	Results and discussion	55
7.1	Validation of the simplified 2D-model	55
7.1.1	Model 1.0	55
7.1.2	Model 1.1	59
7.1.3	Overall assessment of the validity of model 1	61
7.2	Fluid-structure interaction on a simplified 3D-model	61
7.2.1	Results for E equal to 0.45 MPa	63
7.2.2	Results for E equal to 0.518 MPa	65
7.2.3	Results for E equal to 3.33 MPa	67
7.2.4	Preliminary summary for model 2	69
7.2.5	Velocity for E equal to 0.45 MPa, 0.518 MPa and 3.33 MPa	70
7.2.6	Overall assessment	74
7.2.7	Summary	76
7.3	Real geometry with fluid structure interaction	77
7.3.1	Possibilities with a functioning model	79
8	Concluding remarks	80
9	Further work	81
	Nomenclature	82
	References	85
A	Additional results for model 2	A.1

1 Introduction

1.1 Background

Occasionally, young and otherwise healthy individuals experience that their ventilation capacity during physical exercise is limited. Some of those individuals experience that respiratory symptoms persist despite access to asthma treatment and medication.

The term airway obstruction is defined as a condition where the free passage of air to and from the lungs air bags (alveoli) is reduced or prevented [1]. A blockage of the respiratory tract usually leads to breathing difficulties with resulting respiratory sounds as wheezing or gasping for air, and choking. Symptoms like chest pain, agitation and panic is also seen [2].

Various forms of airway obstruction occur with subsequent different classifications. Broadly they can be classified as upper airway obstruction and lower airway obstruction [2]. Furthermore, distinction is made between an exercise-induced obstruction, and an obstruction provoked without exercise.

Exercise induced laryngeal obstruction (EILO) is suggested as one possible diagnosis of certain unexplained respiratory symptoms among individuals struggling with unexplained breathing problems during exercise. An appropriate diagnosis is essential for treatment and thereby for the opportunity to continuously conduct training, both for individuals in general and for professional athletes [3].

The prevalence of EILO is estimated to be 6-8 % for young people in general, while it is predicted to affect 35 % of individuals among all athletes struggling with unexplained respiratory symptoms. The condition is most widespread amongst adolescents, and females are most commonly affected [3].

Exercise-induced symptoms are commonly caused when the breathing rate increases. Normally, the cavity in the larynx expands during exercise, allowing increased airflow. For patients with EILO, the larynx appears ordinary at rest, but an inappropriate obstruction occurs during strenuous exercise. Inspiratory supraglottic collapse, glottic adduction or a combination of both causes the obstruction and thereby the condition of breathing problems [3].

As the EILO phenomenon is not well explored, there are many questions related to both the diagnosis and treatment. The diagnosis is carried out by a continuous laryngoscopy exercise (CLE) test validated for this purpose,

which enables visualization of the larynx during strenuous exercise [3]. By using a thin, flexible tube with a camera lens at the end (called a laryngoscope), visualization of what provokes the laryngeal obstruction is enabled, and furthermore if and how the vocal cords contribute to an increased degree of obstruction. Affected individuals are usually firstly sent to a specialized speech therapist, as lack of control of the vocal cords may increase the symptoms. Fear and anxiety are also suggested as reinforcing factors. This explains the two most common reasons for why speech therapy has proven to be effective for many of the affected individuals [4].

If the problem persists, a new CLE test is conducted, and the need for a surgical intervention is considered. There is currently limited guidance of how to classify the individuals with regards to physical properties. Hence, there is no clear level of restrictions that indicate if the state of the individual qualifies for surgery or not. Actually, only a few hospitals in the world have the appropriate expertise, so there is a lack of capacity to conduct surgical treatment on all individuals who may profit from such. Available information indicates that severity observed and the motivation of the individual forms the basis for deciding adequate treatment. Furthermore, there are no published reports describing the long-term effects of surgical treatment of EILO [5].

1.2 Motivation

As of today EILO is a fairly recognized condition among medical experts in certain countries. However, there is little knowledge of the causes of the phenomenon. Possible causes discussed by Maat [5] relates to heritage, life style and/or a changing perception of the disease. All in all, there is a lack of understanding about which physical parameters that are critical for individuals experiencing EILO. More research is important in order to increase the evidence base for treatment of the diagnosis. An increased understanding of which criteria to focus on during treatment is also essential [4]. Hence it is desirable to obtain a better understanding of why some individuals are affected while others are not.

One step in that direction can be to provide basis for improved understanding of the fluid flow and corresponding properties observed during laryngeal obstruction by the development of a numerical simulation model. With the appropriate assumptions and approximations there is a good correspondence between numerical calculations and experimental results for respiratory phenomena [6]. This indicates that computational fluid dynamics (CFD) simu-

lations are a good alternative to accurately calculate the aerodynamic flow characteristics of the upper airways [4].

Both the engineering and the medical community have become significantly more interested in CFD throughout the last decades. By using numerical simulations one can easily change one or multiple input flow variables to indicate how the fluid flow characteristics will be affected. Moreover, it allows investigation of different flow variables and fluid forces [6].

1.3 Objective

The topic of this thesis is the exercise-induced upper airway obstruction, describing air flow obstruction in the larynx during exercise in patients with no obvious pathology at rest [4].

Hence, the objective of this thesis is to make a CFD model describing an exercise induced laryngeal obstruction (EILO), occurring in the throat during exhaustion. The numerical simulations are carried out by use of the commercial code, STAR-CCM+.

The simulations were divided into three main models:

- **1: Validation of a simplified 2D-model**
Results obtained by Lacis [7] were reconstructed in order to validate the simulation model and programme.
- **2: Fluid structure interaction on a simplified 3D-model**
The simplified 2D-model was extended to 3D, and a fluid-structure interaction was implemented into the simplified 3D-model. The magnitude of Young's modulus varied, to see how it affects the air flow.
- **3: A real geometry from a horse studied in a static situation**
Real geometry data was segmented and moved into the software in order to study the situation in a real throat.

2 Short description of medical background

2.1 Basics of the laryngeal structure

In order to understand the problem considered in the present work, the structure of larynx is presented in this section.

The respiratory system consists of a conducting zone, where the respiratory organs form a path to conduct the inhaled air into the deep lung region, and a respiratory zone, where the gas exchange takes place. The larynx is located in the conducting zone, ranging from nose to bronchioles, as illustrated in figure 2.1. Larynx is the narrowest passage of the airway tree, connecting the hypopharynx with the trachea [8].

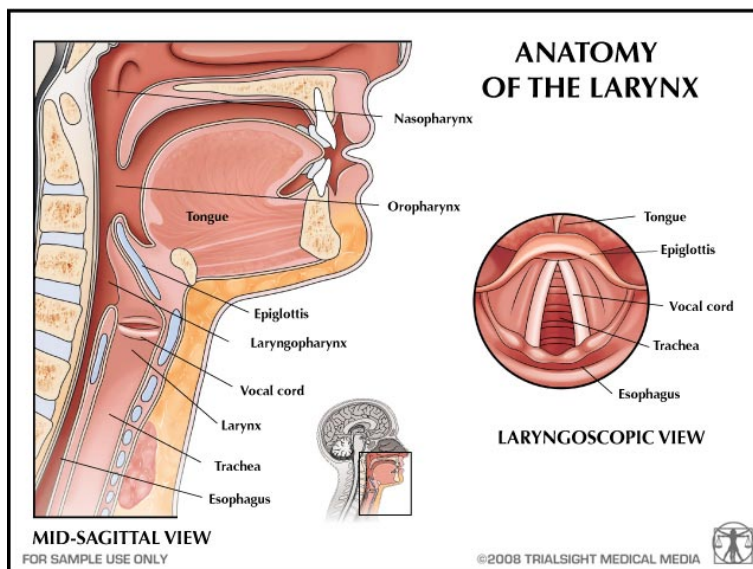


Figure 2.1: Anatomy of the larynx. Image from [9].

As figure 2.2 illustrates, the laryngeal skeleton has a complex structure, consisting of nine cartilages connected by membranes and ligaments. Epiglottis is the major cartilage of the larynx. With its flexible, leaf-shaped structure it spreads over glottis to prevent food or other foreign objects to enter, in order to hinder choking and to protect the airways. This happens automatically during swallowing by pushing the back of the tongue upwards, forcing the epiglottis to close over the glottis. However, epiglottis normally resides in an upright position, allowing air to pass freely through the larynx during inhalation and exhalation [8].

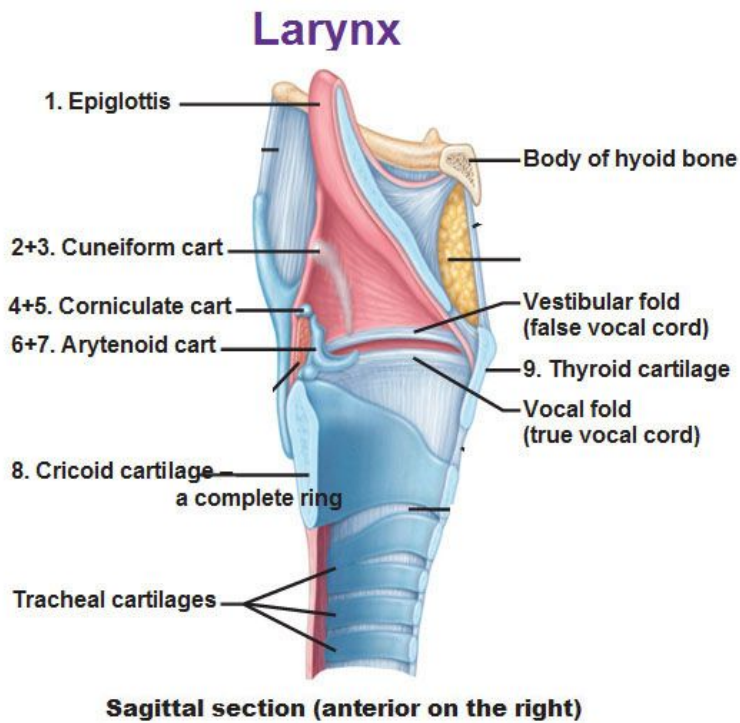


Figure 2.2: The complex structure of the larynx. Image taken from [10].

The vocal folds are also located in larynx, making sound production possible. When air flows through larynx it assist the vocal folds to vibrate against each other. When the vocal cord gap is reduced to a point where the air flow creates and sustains a vocal cord vibration, sound is produced. The vocal cord gap is usually very wide during physical activities, which is favourable for a big volumetric air flow [8].

During physical exercise, the larynx normally opens fully allowing for increased air flow with the least possible increase of air flow resistance [4].

2.2 Exercise induced obstruction

Amongst various forms of exercise induced airway obstructions, exercise induced asthma (EIA) is the most widespread phenomenon and the most commonly used diagnosis for healthy young people. The affected individuals experience an airway obstruction inside the thoracic cage during exercise, producing expiratory symptoms such as coughing, wheezing, shortness of breath and chest pain [4].

In addition, there are numerous other types of exercise-induced obstructions of the central airways, but all of them are less known [4]. One of them is exercise induced laryngeal obstruction (EILO), which is the main topic for this thesis, and is therefore elaborated on in the next section.

2.3 Exercise induced laryngeal obstruction

The term exercise induced laryngeal obstruction (EILO) describes laryngeal air flow obstruction during exercise in patients with no obvious laryngeal pathology at rest [4]. The phenomenon occurs outside the thoracic cage, characterized by a produced air flow obstruction during inhalation.

In contrast to EIA where the symptoms are predominant after 15 minutes, with EILO one experiences symptoms of the airway obstruction especially towards the end of the effort, and 2-3 minutes after the activity has stopped. EILO is characterized by wheezing in the inspiratory phase, making it difficult to retract enough air. In some cases it may also cause noise on the vocal cords [4].

Based on the presented symptoms alone, it is challenging to distinguish EIA from EILO, making it difficult for the medical doctors to recognize it. This may lead to diagnostic errors and inadequate treatment, especially for patients having EILO due to less knowledge about that diagnosis. To diagnose EILO one must perform a laryngoscopic test, using transnasal flexible laryngoscopy continuously throughout an incremental exercise test from rest to exhaustion. Important information for further handling and treatment can be provided during the test, if EILO is recognized [11].

Glottic or supraglottic EILO

Røksund et al. [11] suggest that EILO should be divided into two classes for persons without obvious laryngeal pathology at rest: (i) glottic and (ii) supraglottic, illustrated in figure 2.3. For the glottic EILO the obstruction is located in the glottis region, caused by reduction of the space between the vocal folds. In supraglottic EILO an obstruction is created when the epiglottic fold (more specifically known as cuneiform cartilage/tubercle) bends down and reduces the supraglottic region, as the laryngoscopic view in figure 2.4 illustrates. A scoring system for movements of the laryngeal structure during exercise is illustrated in figure 2.5.

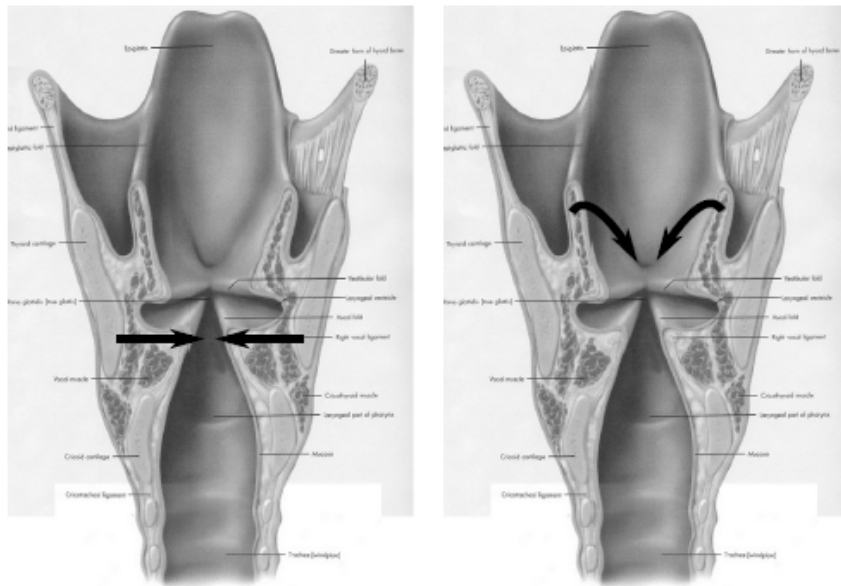


Figure 2.3: A vertical cross-section of larynx. Glottic EILO illustrated on left, while supraglottic EILO is shown on right. Picture from Lacic [7].

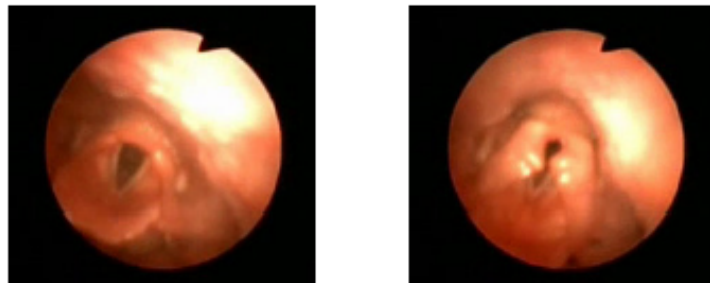


Figure 2.4: The picture on left shows the supra-glottic condition in an open state, while a supra-glottic obstructed condition is shown in the right picture. Images are taken from Lacic [7].

Even though the nature of the supraglottic and glottic EILO is different, both causes respiratory issues and inability to continue exercising. Supraglottic EILO is the most common laryngeal adduction, while glottic EILO is less frequent. However, they often occur as a combination, normally starting with a supraglottic adduction followed by a glottic contraction [11]. This study focus on supraglottic EILO, labeled as EILO from now on.








Glottic (vocal cords) movements		Supraglottic movements	
<p><i>Normal:</i> abduction or neutral position of the vocal cords.</p>		<p><i>Normal:</i> abduction or neutral position of the aryepiglottic folds with no visible medial motion.</p>	
<p><i>Mild:</i> mild adduction of the vocal cords, particularly in the anterior part.</p>		<p><i>Mild:</i> mild medial rotation of the cranial edge of the cuneiform tubercles.</p>	
<p><i>Moderate:</i> moderate adduction of the vocal cords but no direct contact.</p>		<p><i>Moderate:</i> moderate medial rotation of the cuneiform tubercles, exposing the mucosa of the lateral side of the tubercle.</p>	
<p><i>Severe:</i> severe inspiratory adduction of the glottic space, nearly always accompanied by severe stridor.</p>		<p><i>Severe:</i> severe medial motion of the cuneiform tubercles towards the midline, thereby partly covering visual access of the glottis.</p>	

Figure 2.5: Scoring system for movements of laryngeal structures during exercise. Glottic movement is shown in the left column, while supraglottic obstruction is shown on the right hand side. Image taken from Røksund et al. [11].

2.4 Air flow dynamics and resistance

Normal breathing consists of an inhalation process and an exhalation process. Several breathing muscles control the inhalation process, where the diaphragm is the most important. During inhalation this muscle is contracted and flattened, allowing thorax to expand. As a result, the pressure in the lungs and thorax decreases relative to the atmospheric air pressure, so that the atmospheric air from the outside is sucked into the lungs with lower pressure to equalize the difference in pressure [8].

Hence, the pressure difference is the driver of the air flow through the respiratory system. When glottis opens in larynx during respiration, gas flow is allowed to enter the lungs from the upper respiratory system. The flow can be laminar, transient or turbulent, but usually it occurs as a combination of these flow regimes [8]. The Reynolds number gives an indication of the dominating flow regime, and is known as a useful tool to classify different types of flow. The parameter is dimensionless, and is given by:

$$Re = \frac{\textit{inertia force}}{\textit{friction force}} = \frac{\rho Du}{\mu} = \frac{Du}{\nu}, \quad (2.1)$$

where ρ is the fluid density, D is a characteristic diameter or length, u is the fluid velocity, μ is the dynamic viscosity of the fluid and ν is the kinematic viscosity of the fluid.

The internal flow in the respiratory airway may experience both laminar and turbulent flow at low respiratory rates. The influence of the geometry will increase as the flow rates increases, and the inertia forces becomes more dominant. When the motion of the flow is sufficient chaotic and random, turbulent flow occurs [8].

3 Literature study

Despite numerous studies conducted regarding obstructions in the throat in general, knowledge of exercise induced obstructions is limited. Exercise induced asthma is a well known phenomenon, but during the last two decades there has been increased professional awareness and agreement regarding numerous other forms of obstructions, which needs further exploration. In this chapter relevant experimental, numerical and combined studies are presented, as basis for choices and values to be used as basis for the numerical simulations.

3.1 Experimental studies

Eckel et al. [12] performed experiments on the human larynx in order to improve their knowledge of the size, the proportions, its cartilaginous components and the laryngeal framework as a whole. They performed 95 different measurements in each larynx, carried out on 53 adults, without any indications of laryngeal disease. Their experiments contributed to a precise knowledge of the anatomical structure of the larynx, which is an important precondition of any surgical intervention. Reliable information of the proportions of the geometry in larynx is also essential for computer simulation purposes. Eckel et al. obtained experimental data giving the height of the larynx, vocal cord dimensions, inner and outer diameter of the cricoid, shown in figure 3.1.

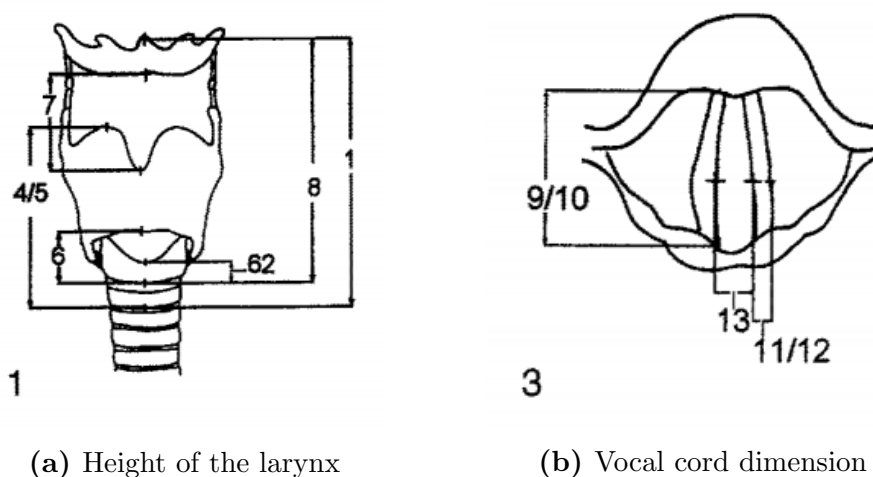


Figure 3.1: Important laryngeal parameters. Images from Eckel et al. [12].

Trabelsi et al. [13] performed histological analysis to characterize the tissues and its mechanics, conducted on three human trachea specimens obtained from autopsies. The aim of their work was to find out how the human trachea responded mechanically under static tensile conditions. The tracheal cartilage was considered an elastic material, decided through uniaxial tensile tests performed on cartilage rings. A Neo-Hookean model was proposed to describe the elastic behaviour, used to fit the experimental curves for the elastic material to an elastic model. For cartilage, like the epiglottic fold, a Young's modulus equal to 3.33 MPa was obtained.

Shinwari et al. [14] studied intraglottal pressures and glottal jet flow in a divergent glottis. They used a plexiglass model of the larynx with similar vocal folds, a constant glottal diameter equal to 0.04 cm and an included divergent glottal angle of 10 degrees. Glottis was symmetric for one case and had an obliquity of 15 degrees for another. Both of the geometries were tested for different transglottal pressure drops. The flow was visualized using a laser sheet, and seeded air flow indicated where the flow separated inside glottis. Their results suggest a difference in the separation point for the flow in the two different cases.

Passman et al. [15] investigated mechanical properties of the laryngeal cartilage of 11 Thoroughbred and Standardbred racehorses, to improve the understanding of the biomechanics of laryngeal function and morphology. A total of 5 specimens were mechanically tested in each horse, to calculate the modulus and permeability of the tissue. Their results suggested relatively straight walls for cricoid when comparing to the morphology of a human. Furthermore, they discovered an increase in modulus for crocoid cartilage equal to 0.13 MPa per year, in addition to a great symmetry between the left and right side of the larynx.

3.2 Numerical studies

De Vries et al. [16] presented a new numerical model of the vocal folds. Initial glottal gaps and subglottal pressures were changed to produce glottal waves. The parameters affected by these waves, such as fundamental frequency, glottal peak flow and phonation threshold pressure were tested for both incompressible Navier-Stokes equations and Bernoulli-equation, and the results were compared with known values from literature. Their studies concluded that applying the Navier-Stokes equations will increase the glottal peak flow by a factor of 2, compared to the glottal peak flow reached when using the Bernoulli-based model. Difference in description of viscous

losses was suggested as an explanation as the Bernoulli-based requires additional calculations to consider the viscous effects, while the viscous effects are included in the Navier-Stokes equations. Hence, they suggested to apply Navier-Stokes equations to achieve an accurate flow description [16].

Gökcan et. al [17] designed a computational 3D-model of the larynx based on selected images from a computed tomography (CT) archive. The aim of the study was to test the laryngeal respiratory cycle and see how the laryngeal structures influence the effectiveness of airflow. A simulated air flow in a model where only glottis geometry was disturbed (called congenital glottic web) was used for comparison with a normal larynx model. Respiratory data from a real individual were used to simulate unsteady air flow through the larynx. They discovered a glottic area for the normal larynx approximately twice the size of the larynx for a congenital glottic web patient, as illustrated in figure 3.2. In the normal larynx, the velocity contours and streamlines were uniform. However, the flow was separated at the glottis level for the congenital glottic web case, producing areas of stagnation in the subglottis and trachea during inspiration. Their study suggests that the cross-sectional area of the flow conduit may be reduced due to the vortex structures created when the flow is separated [17].

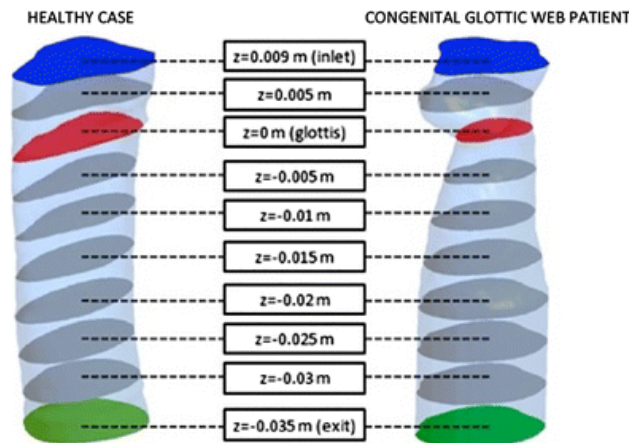


Figure 3.2: A cross-sectional area for a normal larynx model (left) and for a congenital glottic web patient (right). The glottic area of the congenital glottic web patient is half of the size for a normal larynx model. Picture taken from Gökcan [17].

Hundertmark-Zausková et al. [18] performed a set of numerical simulations of the glottal flow during the respiration process for compressible Navier-Stokes equations to find an optimal geometry of the larynx. Several geometrical

models were studied for inspiration and expiration by varying the distance of the vocal folds, thickness of the false vocal folds and the distance between the vocal fold and the false vocal fold. The results of the simulations were compared with respect to air volume and flow resistance after passing the modified vocal folds. Their studies showed no unique optimal geometry for reducing the resistance and increasing the flow rate at once.

De Backer et al. [19] examined whether an upper airway model combining imaging techniques and CFD allows for a prediction of treatment outcome with mandibular advancement devices (MADs), a treatment used for individuals suffering with sleep-disordered breathing. They tested ten patients with and without the MAD, and compared the change in upper airway volume and anatomical characteristics through flow simulations in CFD based on CT images before and after the treatment. The results indicated that a decrease in upper airway resistance, and increase in upper airway volume correlate with both a clinical and objective improvement. As the flow models were based on a patient specific geometry and patient specific boundary conditions, the study suggests that the outcome of the treatment device can be predicted using CFD with an appropriate upper airway model.

Gökcan et. al [20] performed a computational study on the characteristics of air flow in bilateral abductor vocal fold immobility (i.e. forced inspiration draws vocal folds together and closes off the laryngeal inlet). They evaluated airway sufficiency and air flow dynamics in a group of patients who underwent a specific treatment procedure called posterior transverse laser cordotomy (PTLC). The airways was evaluated objectively, and glottic areas were measured from CT images. Comparison of velocity, static pressure, turbulence intensity, and wall shear stress distribution were made between selected cases and a control case. The comparison showed that aerodynamic properties of the larynx are altered due to loss in muscular tonus, in addition to obstruction at the glottic level. As the flow patterns and distributions during respiration varied for each patients, they suggested patient-specific models for evaluation and treatment planning of the matter.

Mylavarapu et al. [21] studied the possibilities for using computational fluid dynamics when planning surgical treatment of the human upper airway. A prediction of the outcome of surgical intervention on the flow and airway resistance was favourable, as it may help the surgeon to choose an effective surgical strategy. Real three-dimensional geometrical models was constructed from CT images, used in CFD to obtain flow patterns during inspiration and expiration. Associated values for velocity, pressure and airway resistance were added, before the virtual surgery based airway models were compared

with the pre-treatment flow modeling results. Their studies concluded that predictions of airway resistances and other numerical calculations from different virtual surgeries give additional inputs for the surgeon, in deciding the most appropriate surgery on a case-by-case basis.

Mihaescu et al. [22] studied the velocity and pressure fields in an unsteady intra-glottal, three-dimensional, symmetric and static laryngeal model of the true vocal folds. Through a numerical study using large eddy simulation (LES) approach they concluded that intra-glottal vortices form in the divergent glottis. The vortices increase the negative aerodynamic pressure and generates a contraction force leading to an acceleration of the closing phase of the vocal cords.

Sul et al. [23] performed a computational study of the respiratory air flow characteristics in the lungs for normal and obstructed human airways. The differences in air flow patterns were characterized through a correlation coefficient for each of the three-dimensional models studied. The results indicated a clear difference in air flow patterns for normal and diseased conditions for high expiratory flow rates, but not for inspiratory flow rates. The results for wall shear stress showed dependence on breathing rates as well as distribution of obstructions in the lung. As a conclusion they suggested that their computational model enabled the study of air flow characteristics that may be impractical to assess experimentally.

Rakesh et al. [24] developed an equine upper airway model for Thoroughbred racehorses to provide insight into general flow patterns and identify susceptible regions to dynamic collapse. Based on CT images from a Thoroughbred racehorse, a fluid mechanics model was created in CFD to make simulations of an in vivo geometry possible. Airway pressure traces from a real horse was set as boundary conditions, while wall pressure turbulent kinetic energy and velocity distributions were studied through simulations. A great correlation between the observed air flow velocity and static tracheal pressure and literature was obtained. Their studies support that the findings from Mylavarapu et al. [6](described in section 3.3), yielding that the area of highest turbulence during inhalation is in the larynx, also applies for horses.

Lacis [7] used computational fluid dynamics to study flow properties for various epiglottic fold shapes of relevance to supra-glottic and glottic exercise induced laryngeal obstructions (EILO). Incompressible, steady Navier-Stokes equations were used with a standard κ - ω model to predict air flow in the larynx. Relations between various epiglottic fold geometries and the resulting flow rates through the larynx was tested for a constant lung suction pressure,

using the numerical simulation program COMSOL. His simulations showed a decrease in flow rate for cases with a blocked larynx. However, he observed an increase in flow rate for cases where the larynx was partially blocked. His simulations also indicated an increase in resulting flow for cases where the distance between the epiglottic fold and vocal chords were increased.

3.3 Combined studies

Mylavarapu et al. [6] evaluated the validity of different turbulence models for the air flow in the upper human airways. They created a model using computational fluid dynamics in addition to a physical model, based on magnetic resonance imaging (MRI) scans from a real person. With both models in place, they implemented different types of turbulence models, and compared the results with the experimental data. Pressure and velocity were measured at multiple points in the larynx, with a flow rate, Q equal to 200 l/min applied. Their results showed the least correlation between numerical and experimental work at the narrowest part of the airways. The standard κ - ω model generally resulted in best agreement with the static pressure measurements, with an average error of 20%. A good correlation between the computations and the experimental results was found, indicating that CFD simulations presents aerodynamic flow characteristics properly [6].

According to Zhang and Kleinstreuer (2003) referred to in [8], the low Reynolds number κ - ϵ model fails to simulate the transition to turbulent flow. Due to the present of laminar, transitional and turbulent flow regimes in the respiratory system, the κ - ω model appeared to be the model to reproduce the behaviour. The LES model is also an applicable alternative handling all flow regimes, but it requires a sufficiently fine mesh to capture the relevant flow features, making this model unfavourable due to its limitations. Based on this, the low Reynolds number κ - ω model is assumed to be the most suitable turbulence model when modeling the upper airways [8].

Liu et. al [25] numerically investigated a realistic human upper airway model. Aiming to study the air flow dynamics in both the inspiration and the expiration process, they reconstructed CT-scan images of a Chinese male patient to create a model. The LES method was applied for the CFD solver to simulate whether the air flow in an obstructed airway for various respiration intensities was laminar, transitional or turbulent. Their investigation discloses that their human upper airway model showed an unsteady transitional/turbulent flow with low Reynolds number. They also found a strong flow injection phenomenon caused by narrowing of the airways in both inspiration and

expiration. Additionally, they discovered that the air flow dynamics were greatly affected by respiratory intensity.

According to Li et al. [26] intraglottal pressure distributions depend upon glottal shape, size and diameter. Nine glottal angles were tested to check how they affected the intraglottal and transglottal pressures. They supported the empirical data with computational results. Their results suggested that the intraglottal pressures on the vocal cords increased when the glottal angle was enlarged. However, a reduced angle resulted in a greater flow resistance. Furthermore, uniform glottis gave the greatest flow resistance, while a 10 degrees glottis gave the lowest flow resistance. An angle of 10 degrees also showed the greatest negative pressure in the glottis, implying a correlation between high negative pressure and low flow resistance. Their simulations indicated that the separation of flow in glottis was moved upwards when the flow and the glottal angles were increased.

4 Basic computational fluid dynamics

When trying to predict how the air flow in the larynx behaves during EILO, the fluid flow equations and the equations of motion in the solid structure must be solved. In this chapter, a brief introduction of the basic principles used in the numerical simulation process is outlined.

Computational fluid dynamics (CFD) is mainly used as a research tool in fluid mechanics, and to help interpret and understand the results of theory and experiment. Numerical simulations are used in order to analyse and solve problems involving fluid flow. One important advantage of using CFD is the higher degree of information obtained during simulations, compared to e.g. experimental techniques [27].

CFD uses computers to solve mathematical models, both integral and partial differential equations, to obtain a solution in different places in space and time in a computational domain. The mathematical equations are based on the following physical conservation laws [27]:

- Conservation of mass
- Balance of momentum
- Conservation of energy

These conservation laws are called the governing equations for fluid flow. If the flow is viscous, the equations are called the Navier-Stokes equations.

4.1 Continuity equation

The first conservation law is called the continuity equation. It is based on the physical principle that mass is conserved, meaning that for any element of fluid [28]:

$$\begin{aligned} & \textit{Rate of mass flow in} - \textit{rate of mass flow out} \\ & = \textit{rate of mass accumulation} \end{aligned}$$

For a finite control volume fixed in space, the following continuity equation

in conservation form is used [27]:

$$\frac{\partial}{\partial t} \iiint_V \rho \, dV + \iint_S \rho \mathbf{V} \, d\mathbf{S} = 0, \quad (4.1)$$

where the first term denotes the time rate of decrease of mass inside V , and the second term represents the net mass flow out of the entire control volume through control surface S , integrated over the entire surface S .

The integral form of the equations allows for the presence of discontinuities inside the fixed control volume, making it valid for both continuous and discontinuous flow.

This equation can also be expressed on differential form:

$$\frac{\partial \rho}{\partial t} + \nabla \cdot (\rho \mathbf{V}) = 0, \quad (4.2)$$

where ∇ is a vector operator, defined as

$$\nabla \equiv \mathbf{i} \frac{\partial}{\partial x} + \mathbf{j} \frac{\partial}{\partial y} + \mathbf{k} \frac{\partial}{\partial z}. \quad (4.3)$$

The infinitesimally small aspect of the element explains why the equation is obtained directly in partial differential form [27].

4.2 Momentum equation

The balance of momentum is based on Newton's second law of motion and states that:

$$\sum F_x = ma_x, \quad (4.4)$$

where the left hand side represents the sum of the forces acting on a control volume, comprised of body forces and surface forces acting on the volume. The body forces act over the entire volume and usually includes gravity, centrifugal, Coriolis and electromagnetic forces. Surface forces are the forces acting on the surface of a fluid element, causing it to deform. The contributors to surface forces are normal stress, a combination of pressure exerted

by the surrounding fluid and normal viscous stress components that act perpendicular to fluid element surface, and tangential stresses acting along the surface of the fluid element [8].

The total force in x-direction, comprised of body forces and surface forces, is given by:

$$F_x = \left[-\frac{\partial p}{\partial x} + \frac{\partial \tau_{xx}}{\partial x} + \frac{\partial \tau_{yx}}{\partial y} + \frac{\partial \tau_{zx}}{\partial z} \right] dx dy dz + \rho f_x dx dy dz. \quad (4.5)$$

The right hand side of the equation describes the time rate of change of momentum for a control volume. It consists of the mass of the control volume, m :

$$m = \rho dx dy dz, \quad (4.6)$$

times the acceleration of the control volume, a :

$$a_x = \frac{Du}{Dt}, \quad (4.7)$$

where $\frac{D}{Dt}$ is the substantial derivative, defined as

$$\frac{D}{Dt} \equiv \frac{\partial}{\partial t} + u \frac{\partial}{\partial x} + v \frac{\partial}{\partial y} + w \frac{\partial}{\partial z}. \quad (4.8)$$

By combining Eqs. (4.4), (4.5), (4.6) and (4.7), the momentum equation in x-direction for an infinitesimal fluid element moving with the flow is obtained:

$$\rho \frac{Du}{Dt} = -\frac{\partial p}{\partial x} + \frac{\partial \tau_{xx}}{\partial x} + \frac{\partial \tau_{yx}}{\partial y} + \frac{\partial \tau_{zx}}{\partial z} + \rho f_x. \quad (4.9)$$

In other words, Eq. (4.9) shows a partial differential momentum equation in non-conservation form. Similar equations can also be derived for y and z direction [27].

4.3 Energy equation

The first law of thermodynamics forms the basis for conservation of energy as it states that the total energy content of a control volume does not change during a steady flow. In other words; energy is conserved in an isolated system. This implies equality between the amount of energy entering a control volume and the amount leaving it. Thus the rate of change of energy in the control volume is equal to the net rate of heat added to the fluid element plus the net rate of work done by body and surface forces on the fluid element. The energy term consists of the fluid energy per unit mass, whereas the net rate of heat added is based on Fourier's heat conduction equation. The rate of work done by the body force consists of the force, multiplied by the component of velocity in the direction of the force [8].

In this thesis, the incompressible Navier-Stokes equations apply. Hence, the energy equation is not involved in the solution process.

4.4 Wall boundary conditions

Although the governing equations are the same for all flow fields, the flow behavior in each case can be quite different. The explanation can be found through the boundary conditions, which depend on the physical properties of the fluid and the field involved [27]. The boundary conditions for this thesis can be related to the "laryngeal walls", and also for "inlet" and "outlet" of the throat.

When air flows through the throat, a viscous regime and a no-slip condition will apply. This condition assumes that the relative velocity between the boundary, and the boundary itself is zero. For viscous flow moving past a stationary surface this implies that $u = v = w = 0$ at the surface [27].

According to the no-slip condition mentioned above, the velocity has its highest magnitude in the middle of the tube and decreases towards the wall where the magnitude is zero. Dimensionless parameters are often used to express the velocity distribution in turbulent flows. The following equations are used [28]:

$$u^* \equiv \bar{V} \sqrt{\frac{f}{2}} = \sqrt{\frac{\tau_w}{\rho}} \quad (4.10)$$

$$u^+ \equiv \frac{u}{u^*} \quad (4.11)$$

$$y^+ \equiv \frac{yu^*\rho}{\mu} = \frac{y}{\mu} \sqrt{\tau_w \rho}, \quad (4.12)$$

where \bar{V} is the mean flow velocity, u^* is the friction velocity, u^+ is the velocity quotient, y^+ is the distance and y is the distance from the wall of the tube. Both u^+ and y^+ are dimensionless parameters. τ_w is the shear stress at the pipe wall and f is the friction factor. Equation 4.12 is based on the friction velocity and the wall distance, and is an equivalent of the Reynolds number.

The wall region can be divided into three regions, namely [28]:

- The viscous sublayer: $y^+ < 5$, where $u^+ = y^+$
This is the inner layer of the wall where the velocity gradient is nearly constant and the flow behaviour is viscous most of the time. This layer is usually relatively thin, with infrequent turbulent eddies and the viscous shear dominates.
- The buffer zone: $5 < y^+ < 30$, where $u^+ = 5.00 \ln y^+ - 3.05$
This is the region between the viscous sublayer and the turbulent core, often described as the transition layer. It is known as the buffer layer, as the flow changes from laminar to turbulent in this zone, meaning that both turbulent eddies and viscous shear appears frequently.
- The turbulent core: $30 < y^+$, where $u^+ = 2.5 \ln y^+ + 5.5$
The flow is fully turbulent in this region, meaning that the bulk of the cross section of the flow is occupied by entirely turbulent flow. This layer is often referred to as the logarithmic layer.

As described earlier, the flow is truly turbulent for a high Reynolds number. The viscous sublayer is very thin for such case, so it is difficult to use enough mesh points to resolve it. To avoid this problem, an assumption of a logarithmic region in the velocity profile is applied.

4.5 Discretization

Closed form mathematical expressions are viewed as having an infinite number of values throughout some domain. When an approximation of analogous

expressions prescribes values at only a finite number of discrete points or volumes in the domain, it is said to be discretized. The technique is used to divide a domain into given grid points, as illustrated in figure 4.1. For variables at discrete locations in space and time, the discretization method can approximate differential equations in the mathematical models by a system of algebraic, discrete equations [27].

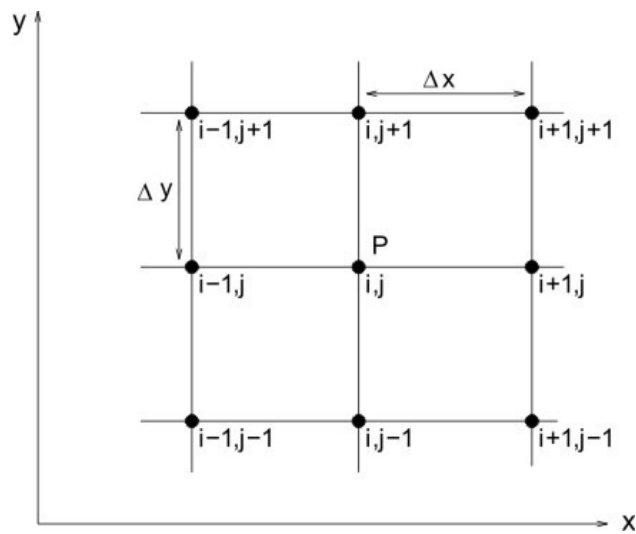


Figure 4.1: Discrete grid points in the xy -plane. Image from [29].

The most used approximation methods are the finite difference (FD), finite volume (FV) and finite element (FE). The software utilized in this thesis is STAR-CCM+, which is mainly based on the finite volume method, but also uses the finite element method in special cases (like solid stress analysis, for instance) [30]. In this thesis, the finite volume method is used to solve the fluid domain, while the fluid element method is used to solve the solid domain. Mapped contact interface allows for data mapping between the finite volume and finite element meshes [31].

Finite volume method

The finite volume method is based on following conservation principle [8]: “The flux of a variable (i.e. net rate of a mass of a variable that crosses the control surface) is equal to the net change in quantity of the variable inside the control volume”. Each control volume has a bounding surface area acting as faces, where the flux of a dependent variable moves across. The

computational domain is divided into a finite number of discrete contiguous control volumes, each volume containing a centroid where the variable values are calculated and stored.

When governing partial differential equations are presented through a system of algebraic equations and then solved through numerical methods, it results in computational solutions to the governing equations. According to Tu et al. [8] the relevance and credibility of the computational solutions can be controlled by a number of analyzes such as consistency, stability and convergence.

The idea of consistency deals with discretization of the partial differential equations, where the approximation can be considered consistent if the truncation error (or consistency error) approaches zero when the mesh size and time step size are reduced. The truncation error represents the difference between the discretized equation and the exact one. In other words, this error determines the rate at which the error decreases as the time step and/or mesh spacing are reduced and shows the accuracy of the approximation [8].

Stability concerns the growth or decay of errors at each step during the computation. A numerical solution method is considered to be stable if it does not magnify the errors that appear during the numerical solution process. In other words, if a numerical solution is stable, then the solution does not diverge [8].

If a numerical method satisfies both consistency and stability, we may conclude that the numerical procedure is convergent. Convergence implies that the solution of the system of algebraic equations approaches the true solution of the partial differential equations as the mesh is refined. If the residuals diminish as the numerical process progresses, convergence is satisfied [8].

4.6 Mesh

Using CFD applications requires proper assumptions and adjustments, in order to achieve reliable results. An essential requirement for obtaining consistent computational solutions is the generation of a quality mesh, in order to increase the numerical stability [8]. A mesh is a way of dividing the appropriate geometry into smaller meshes or grid cells. Each of the grid cells possess a set of fundamental mathematical equations, which calculates the changes in each cell within the domain. These equations represent the flow physics inside of the grids, and give corresponding discrete values of the flow-field variables when they are solved [30].

There are two main classes of mesh systems; structured mesh, containing cells having either rectangular or hexahedral shape, and unstructured mesh comprised of triangles or tetrahedral. For a complex geometry, like a larynx, an unstructured mesh is applied due to its flexibility [8].

Residuals

The numerical solution is highly dependent on the number of cells contained in the domain [30]. This section presents the different aspects and errors associated with the mesh size utilized in the study.

When discrete finite volume equations are applied in the solution domain, it will result in solutions with corresponding error estimations. Each solution domain contains a discretization error, and the error estimate gives an overview of the approximate magnitude and distribution of this error. The error estimates are caused by the mesh spacing, irregularity and non-orthogonality, the arrangement to account for differencing and the size of the time steps used for the calculations [30].

STAR-CCM+ is based on the Residual error estimate method. This method is built on the imbalance between interpolation and volume integrations, and results in a residual in each cell. The residual is then normalized in order to produce the estimate of the absolute magnitude of the error with the same physical dimensions as the variable in question, in order to make the comparison of the two quantities easy [30].

The size of the error is highly dependent on the mesh refinement. When the mesh becomes sufficiently fine to resolve all features of the flow, the error will decrease with the square of the mesh size. When the mesh becomes perfectly fine, the exact error will be approached for the error estimate [30].

5 Additional models applied

5.1 Turbulence models

When the Reynolds number increases, flow streamlines become unstructured, and the flow develops from laminar, to transitional and further to turbulent flow. The flow stream consists of eddies of different sizes, with new eddies constantly formed in a turbulent flow. One distinguish between two types of turbulence: wall turbulence and free turbulence. For a fluid flowing through closed or open channels, or past solid shapes immersed in a stream, wall turbulence will appear [28].

Additional unknowns are added to the system of equations in order to present approximations for the flow field at the walls. The approximations are based on the observation that the turbulent flow field u over time contains small, local oscillations u' that can be treated in a time-averaged sense U . This results in numerous different turbulence models, and Reynolds-averaged Navier-Stokes (RANS) represents the basis for them all. The Navier-Stokes equations are augmented with an extra turbulent viscosity term for each of the models, but their usage and computations differ. The difference lies in their usage of wall functions, the number of additional variables solved for, and what these variables represent [32].

When the continuity and momentum equations are averaged out and the RANS approach is applied, the differential form of the equations becomes

$$\frac{\partial(\rho\bar{u}_i)}{\partial x_i} = 0 \quad (5.1)$$

$$\frac{\partial(\rho\bar{u}_i)}{\partial t} + \frac{\partial}{\partial x_j}(\rho\bar{u}_i\bar{u}_j + \overline{\rho u'_i u'_j}) = \frac{\partial\bar{p}}{\partial x_i} + \frac{\partial\bar{\tau}_{ij}}{\partial x_j} \quad (5.2)$$

where $\rho\bar{u}_i\bar{u}_j$ is the Reynolds stresses. Due to the additional terms and unknowns in the fundamental equations, a turbulence model for the numerical simulations is introduced [33].

5.1.1 The SST κ - ω turbulence model

One of RANS turbulence models is the SST κ - ω turbulence model, classified as a two-equation eddy-viscosity model. It combines the original κ - ϵ , which

accounts for the flow in the outer region and free shear flow, with the Wilcox κ - ω model, describing the flow in the boundary layer [34].

The model requires the shear stress transport (SST) equations for kinetic energy of turbulence, κ , and the specific dissipation rate, ω , to be solved. ω describes dissipation rate per unit turbulent kinetic energy, and is given by ϵ divided by κ . This implies that this model combines the usage of both the κ - ϵ and the κ - ω model to solve the flow field. The κ - ω model has a great ability to be applied throughout the boundary layers, making it accountable all the way from the wall throughout the viscous sub-layer. On the other hand, the model has a huge sensitivity to inlet boundary conditions for internal flows, meaning that the boundary layer computations are sensitive to the values of ω in the free stream. Hence the κ - ϵ model is included due to its advantage to describe the behaviour in the free-stream, so the description of the total flow field is fulfilled. Due to this inclusion, the SST κ - ω model can be used as a Low-Re turbulence model without the need to include any extra damping functions [35].

The kinetic energy of turbulence, κ are calculated from [35]:

$$\frac{\partial k}{\partial t} + U_j \frac{\partial k}{\partial x_j} = P_k - \beta^* k \omega + \frac{\partial}{\partial x_j} \left[(\nu + \sigma_k \nu_T) \frac{\partial k}{\partial x_j} \right], \quad (5.3)$$

and the specific dissipation rate, ω are solved from:

$$\frac{\partial \omega}{\partial t} + U_j \frac{\partial \omega}{\partial x_j} = \alpha S^2 - \beta \omega^2 + \frac{\partial}{\partial x_j} \left[(\nu + \sigma_\omega \nu_T) \frac{\partial \omega}{\partial x_j} \right] + 2(1 - F_1) \sigma_{\omega 2} \frac{1}{\omega} \frac{\partial k}{\partial x_i} \frac{\partial \omega}{\partial x_i}, \quad (5.4)$$

where ν_T is the kinematic eddy viscosity given by:

$$\nu_T = \frac{a_1 k}{\max(a_1 \omega, S F_2)}. \quad (5.5)$$

The coefficients F_1 and F_2 are given by

$$F_1 = \tanh \left\{ \left\{ \min \left[\max \left(\frac{\sqrt{k}}{\beta^* \omega y}, \frac{500 \nu}{y^2 \omega} \right), \frac{4 \sigma_{\omega 2} k}{C D_{\kappa \omega} y^2} \right] \right\}^4 \right\} \quad (5.6)$$

$$F_2 = \tanh \left[\left[\max \left(\frac{2\sqrt{k}}{\beta^* \omega y}, \frac{500\nu}{y^2 \omega} \right) \right]^2 \right]. \quad (5.7)$$

Additional relations required to solve the equations are:

$$P_k = \min \left(\tau_{ij} \frac{\partial U_i}{\partial x_j}, 10\beta^* k \omega \right), \quad (5.8)$$

$$CD_{k\omega} = \max \left(2\rho\sigma_{\omega^2} \frac{1}{\omega} \frac{\partial k}{\partial x_i} \frac{\partial \omega}{\partial x_i}, 10^{-10} \right), \quad (5.9)$$

$$\phi = \phi_1 F_1 + \phi_2 (1 - F_1). \quad (5.10)$$

α_i , β_i , β^* and σ_i represents constants.

5.2 Fluid-Structure Interaction

The lung volume will increase during inhalation, leading to a decrease in pressure relative to the outside air. The pressure difference that occurs will cause the air to move during inhalation, producing air flow. When air flows it causes a stress on the structure which will cause deformations in the solid structure. Furthermore, deformations in the solid structure will affect the air flow, and the process can be categorized as a fluid-structure interaction [36].

According to Tu et al. [8], a fluid-structure interaction (FSI) involves the influence of the moving fluid on a flexible structure which deforms and in turn influences the fluid flow. It occurs when a fluid flow exerts a stress on the structure, which causes it to deform and thereby generate a new geometry for the fluid flow [36].

A CFD model combining dynamic and static mesh can be used in order to solve FSI problems. When structural dynamics equations are coupled with the equations of fluid dynamics, determination of the moving structures is possible. The fundamental equation used to solve a FSI problem is the

Newton's second law applied to a mechanical system, and is the foundation for the coupling technique [37]:

$$m\vec{\Gamma} = \sum_{forces} \vec{F}_i, \quad (5.11)$$

where m is the system mass, $\vec{\Gamma}$ is the acceleration vector and \vec{F}_i is the applied forces like gravity and aerodynamic forces. Each part of the equation is assigned a specialized solver:

- Left term: computed with a structure solver
- Right term: computed with a fluid flow solver
- Equality: a coupling scheme to update common data between the solvers

A suggested solution method consists of relating each part of the equation with a specialized solver, using a coupling technique to provide the equality term.

5.2.1 Structural mechanics

If this method is applied, the left hand side is calculated with a structure solver using an elastic formulation and a non-linear geometry formulation to allow large deformations [37].

The response on the solid structure is based on the stress, strain and deformation properties of the solid material [31].

Stress, σ , is defined as

$$\sigma = \frac{F}{A}, \quad (5.12)$$

where F is force and A is the area the force is applied, as the area shrinks to zero. In other words, it measures the internal forces that arise when a body is deformed, due to external forces. A full stress tensor description is needed to completely describe the stress at a point in any plane:

$$\sigma = \begin{pmatrix} \sigma_{xx} & \sigma_{xy} & \sigma_{xz} \\ \sigma_{yx} & \sigma_{yy} & \sigma_{yz} \\ \sigma_{zx} & \sigma_{zy} & \sigma_{zz} \end{pmatrix}. \quad (5.13)$$

The notation σ_{ij} is consistent with stress acting in the i direction on a plane normal to the j direction. σ_{xy} , σ_{yz} and σ_{zx} act tangentially to the plane and are called shear stresses, while σ_{xx} , σ_{yy} and σ_{zz} are the diagonal terms called normal stress [31].

Strain, ε , describes how much a body deforms from the stress in the material, also known as the relative deformation, and is defined as:

$$\varepsilon = \frac{l - l_o}{l_o}, \quad (5.14)$$

where l is a point in the undeformed body, and l_o is the point in the deformed state. A complete strain description is required and can be given by the strain tensor [31]:

$$\varepsilon = \begin{pmatrix} \varepsilon_{xx} & \varepsilon_{xy} & \varepsilon_{xz} \\ \varepsilon_{yx} & \varepsilon_{yy} & \varepsilon_{yz} \\ \varepsilon_{zx} & \varepsilon_{zy} & \varepsilon_{zz} \end{pmatrix}. \quad (5.15)$$

The deformation of a part is defined by a vector quantity describing how much the part is deformed/displaced compared to its original undeformed shape. If the displacement of the original material point \mathbf{X}_o is $\mathbf{u}(\mathbf{X}_o)$, where \mathbf{u} is the displacement field, the new coordinates of the material point will become $\mathbf{X} = \mathbf{X}_o + \mathbf{u}(\mathbf{X}_o)$. This results in a deformation gradient $\nabla \mathbf{u}$ describing how the deformation changes from point to point [31]:

$$\nabla \mathbf{u} = \begin{pmatrix} \frac{\partial u}{\partial x_o} & \frac{\partial u}{\partial y_o} & \frac{\partial u}{\partial z_o} \\ \frac{\partial v}{\partial x_o} & \frac{\partial v}{\partial y_o} & \frac{\partial v}{\partial z_o} \\ \frac{\partial w}{\partial x_o} & \frac{\partial w}{\partial y_o} & \frac{\partial w}{\partial z_o} \end{pmatrix}. \quad (5.16)$$

The above definitions and equations forms the basis for the structural mechanics being solved in the fluid-structure interaction.

5.2.2 Fluid mechanics

The fluid flow solver is based on the incompressible Navier-Stokes equations, described previously in section 4.1, 4.2 and 4.3. These equations are solved for the velocity and pressure field and represents the right hand side of equation 5.11.

5.2.3 Coupling of fluid and structure

The equality sign indicates the coupling scheme established to update common data between the solvers. Such data correspond to partial pressure and the position and velocity field of the mechanical system, shown in figure 5.1 [37]:

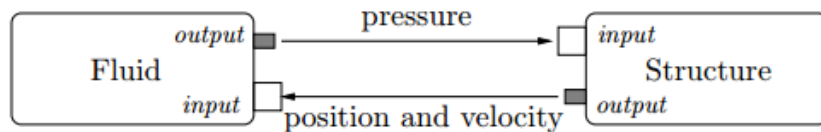


Figure 5.1: Suggested solution method for a fluid-structure interaction. Image taken from Lefrancois [37].

5.2.4 Classifications of fluid-structure interactions

Fluid-structure interactions are normally categorized as either “one-way interactions” or “two-way interactions”. When the fluid imparts some action on the structure, but the response of the structure to the fluid loading does little to affect the fluid motion, it is named as a “one-way interaction”. In other words, even though the motion of the fluid affects the motion of the structure, this structure motion will not affect the motion of the structure further. On the other hand, if there is a mutual effect between the motion of both phases, the flow is said to be two-way coupled [31].

One normally distinguish between a monolithic and partition approach to solve a FSI problem. When the governing equations for flow and displacement of the structure are solved simultaneously, it is named as a monolithic approach. A partition approach solves the equations governing the flow and the displacement of the structure separately [8].

In order to account for the boundary deformations and subsequent deformation of the fluid mesh in the narrowed airway in the larynx, STAR-CCM+ uses an Arbitrary Lagrangian-Eulerian (ALE) description. This method is classified as a monolithic approach as it solves the fluid and structural equations of motion in time simultaneously. The fluid equations are solved in an Eulerian reference frame, so the fluid velocity and the pressure are defined as functions of the space and time coordinates, meaning that the fluid moves

while the mesh remains fixed. The structural equations are solved as a Lagrangian system, so the motion is expressed as displacement from an initial configuration, meaning that the mesh moves with the material [36].

5.3 Elasticity and Young's modulus

The ability of an object to resist a deforming force, and return to its original shape when the force is removed, is called elasticity. When an elastic material is deformed due to an external force, it experiences internal resistance to the deformation and restores to its original state if the external force is no longer applied [38].

If a linear relation between stress and strain applies for an elastic material, the material is said to follow Hooke's law. The law states a relationship between tensile force, F , and corresponding extension displacement, x :

$$F = kx, \tag{5.17}$$

where k is a constant known as the rate or spring constant.

The amount of force per unit area needed to achieve a given amount of deformation is called a modulus, and indicates the amount of elasticity of a material. The greater value of the modulus, the harder is a deformation of the material [38].

Various forms of moduli occur, such as Young's modulus, shear modulus and bulk modulus, all of them are mechanical properties describing the elastic solid materials. The most important modulus for this study is the Young's modulus (also known as the elastic modulus), represented by E . It applies to extension/compression of a body and measures the stiffness of the solid material [38]. An expression between stress, σ , and strain, ε can be used to express the modulus:

$$E = \frac{\sigma}{\varepsilon}. \tag{5.18}$$

The modulus enables calculation of the change in an elastic material under tensile or compressive loads, and predicts how much the material sample will extend under tension, or shorten during compression.

6 Methodology

This section gives a description of the geometries and mesh used in all simulations. Additionally, different models and solvers required to compute the problem at hand are presented.

6.1 Development of model geometries

Model 1 - validation

The geometries used in the simulations for model 1 were designed using the built-in 3D-CAD tool in STAR-CCM+. Model 1.0 consists of a rectangular model, with a narrower section in the middle of the box. The model was constructed by hand and extruded 4 mm to account for the 2D-geometry. Model 1.1 is similar to model 1.0, except that an extra obstacle is added in the model, representing the epiglottic fold, thus a solid part. The interaction between the rectangular model and the epiglottic fold was set to "none", and the subtract feature was used to subtract the epiglottic fold from the rectangular model, to create a model only containing fluid. Figure 6.1 shows the different geometries for model 1, created by the 3D-CAD tool, to represent the simplified geometries used by Lacis [7].

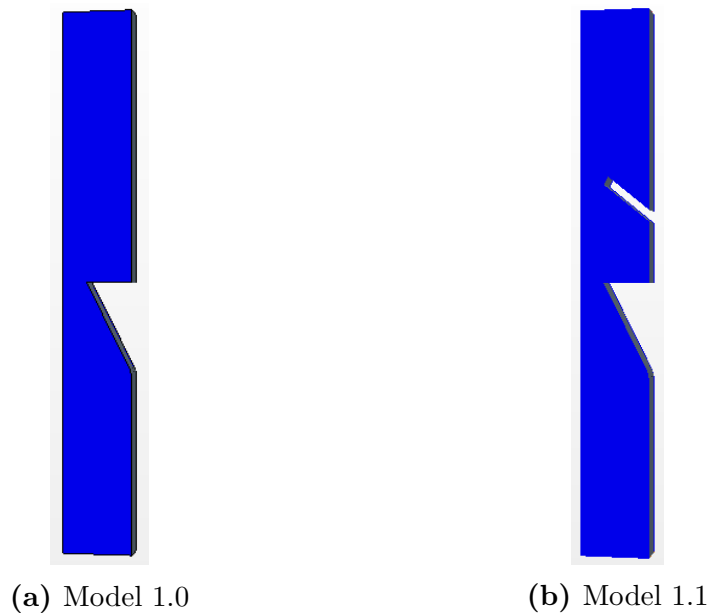


Figure 6.1: Geometries for model 1.

Model 2 - fluid-structure interaction

Model 2 was created in the same way as model 1.1, still using the 3D-CAD tool in STAR-CCM+. However, it was extruded 14.25 mm to become quasi-3D, so that the flow became three-dimensional. A refinement part was also created and extruded with interaction set to "no interaction" in order to improve the quality of the mesh in the most critical region. Figure 6.2 illustrates the geometry for model 2.

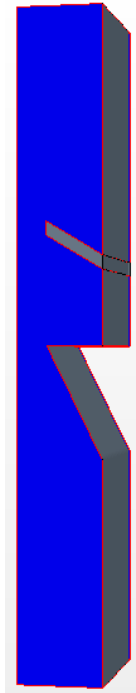


Figure 6.2: Geometry for model 2.

The main parameters in model 2 are taken from Eckel et al. [12] and are carried out as an average of data concerning human larynx. The main length of the larynx is $L_{main} = 71.3$ mm, the main diameter of the trachea is $d_{main} = 18.15$ mm and the vocal cord opening size is $v_{open} = 6.3$ mm. Furthermore, the epiglottic fold distance is found to be $f_{dist} = 8.0$ mm, the epiglottic fold length $f_{length} = 7.0$ mm and the epiglottic fold width is found to be $f_{width} = 1.5$ mm. In addition to this is the depth of the larynx estimated to be $L_z = 14.25$ mm for a rectangular case. Figure 6.3 illustrates the names and locations in the throat for the different parameters described.

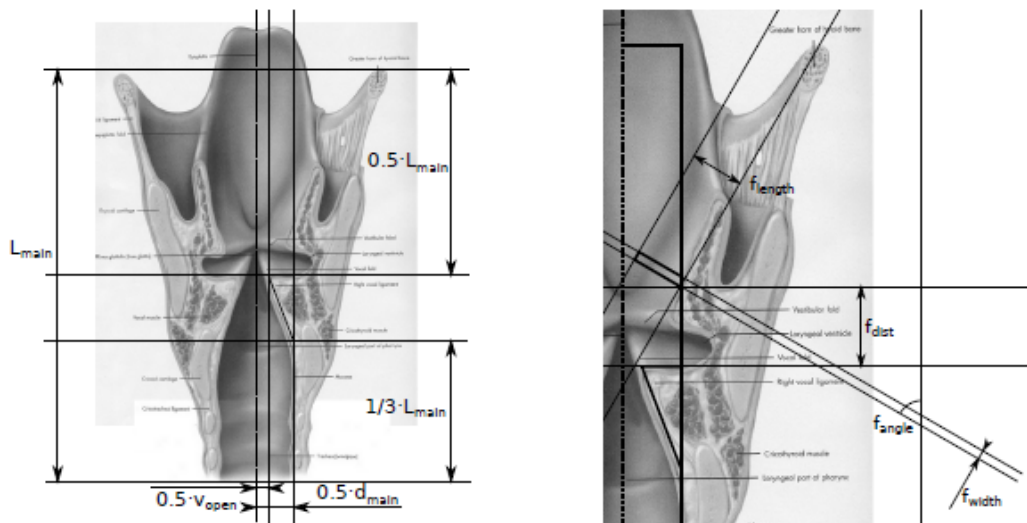


Figure 6.3: Overview of the parameters obtained by Eckel et al. [12]. Image taken from Lacis [7].

Model 3 - real geometry

The real geometry used in the simulations originates from CT-data from a well-known Norwegian Thoroughbred race horse. The original data is in DICOM format, converted to Nifti so it can be read directly into ITK-snap, a software application used to segment structures based on 3D medical images [39]. Figure 6.4 shows a screenshot of the segmentation software, and figure 6.5 displays different viewpoints of the laryngeal structure obtained.

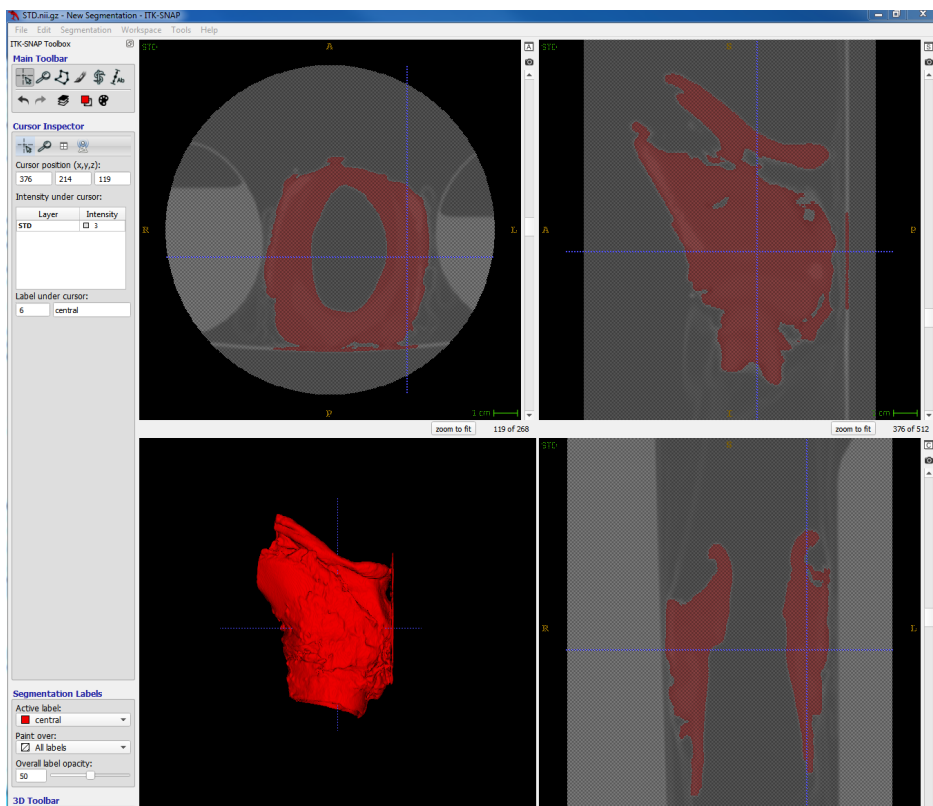


Figure 6.4: A screenshot illustrating what the segmentation software ITK-snap looks like.

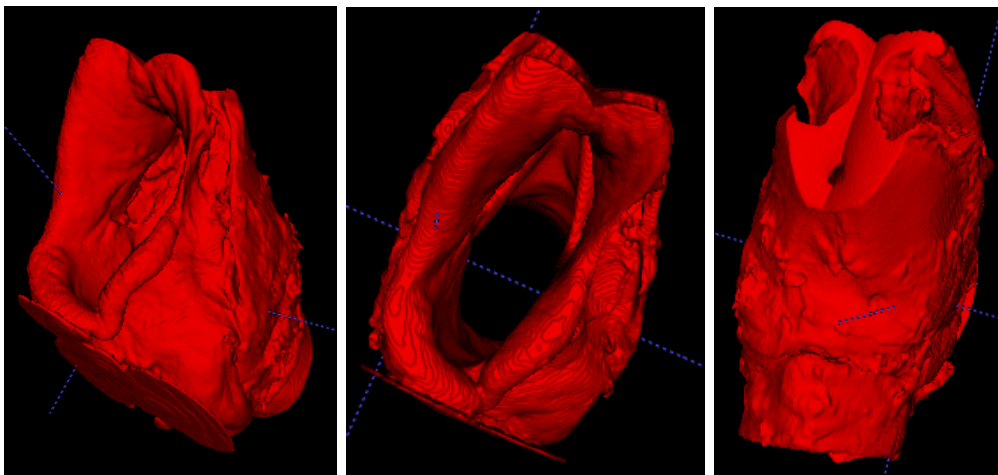
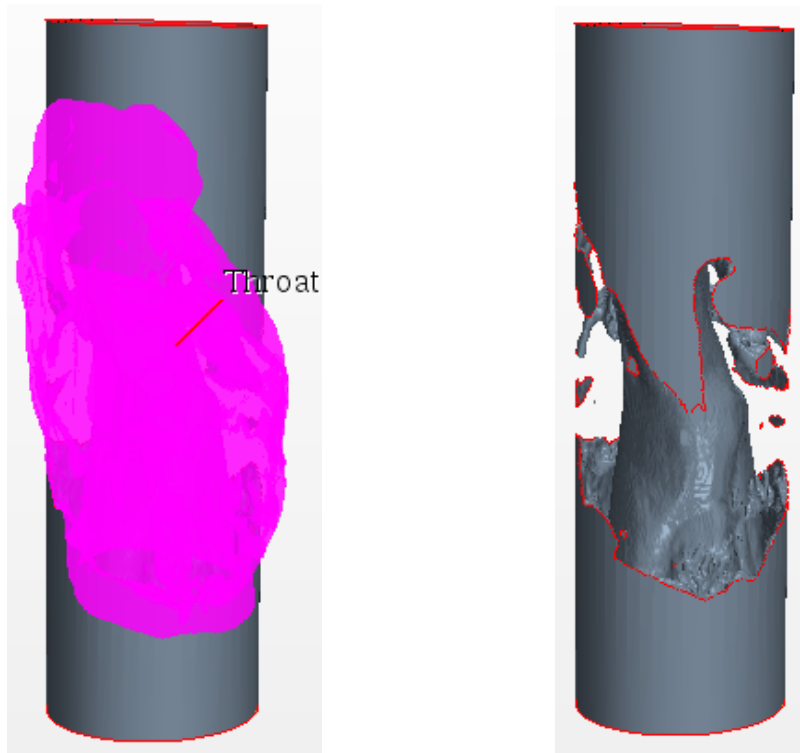


Figure 6.5: Different viewpoints of larynx obtained through segmentation in ITK-snap.

The segmented data obtained by ITK-snap was imported into STAR-CCM+ and formed the basis for model 3. Furthermore, a cylindrical tube with radius equal to 0.03 m was created to enclose the cavity of the throat. The real geometry was subtracted from the cylindrical tube, to obtain a fluid passage to reflect the flow regime in a more realistic throat. The above-mentioned geometry can be seen in figure 6.6, where figure 6.6a illustrates the throat with the enclosing cylindrical part included. Figure 6.6b displays the cylindrical part when the throat is subtracted, constituting the fluid part of the throat, hereby referred to as model 3.0.



(a) Fluid passage with throat

(b) Model 3.0 - fluid passage

Figure 6.6: Geometry for model 3.0.

In addition to this, an extra cylinder with radius equal to 0.055 m was added outside of the region of interest in model 3.0, shown in figure 6.7a. The area between the black, thin lines represents the region of interest, where the fluid flow affects the epiglottic fold and the fluid-structure interaction occur. The subtract feature was used to subtract model 3.0, shown in figure 6.6b, from the newly created cylindrical tube to avoid the presence of fluid in that part. The new cylindrical part obtained represents the solid part in the

fluid-structure interaction. The overall geometry for the above-mentioned description is illustrated in figure 6.7b, hereby referred to as model 3.1.

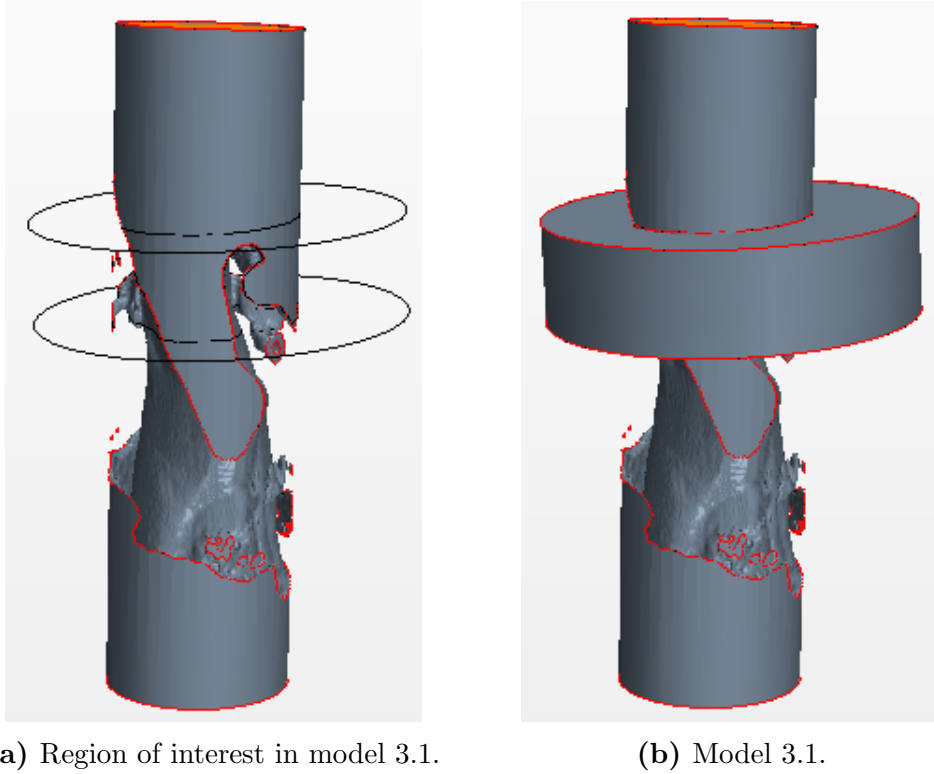


Figure 6.7: Geometry for model 3.1, consisting of the fluid passage (model 3.0) with an added solid part outside of the region of interest.

6.2 Preliminary analysis

According to literature [40], minute ventilation, v_E is determined by the following equation:

$$v_E = v_T \times f_B \quad (6.1)$$

where v_T is the tidal volume per breath and f_B is the frequency of breath per minute. Normally, healthy persons have an average minute volume of 6 l/min at rest, depending on size, age and health status of the individual. However, minute ventilation can increase to over 100 l/min during heavy exercise. On this basis, a constant flow rate equal to 100 l/min is assumed for further calculations.

In this subsection, general flow characteristics such as velocity, Reynolds number and number of steps needed in simulations will be calculated for model 2 and model 3 used in this study. These are necessary parameters for appropriate selection of boundary conditions, and thereby fundamental to enable a realistic CFD simulation of the respiratory system.

6.2.1 Model 2 - fluid-structure interaction

Assuming a cylindrical throat with d equal to 18.15 mm (from section 6.1), the inlet velocity is given by $u = \frac{Q}{A} = \frac{Q}{\pi r^2} \approx 6.44$ m/s.

Furthermore, the narrowest region in the larynx has a diameter, d equal to 6.3 mm, so the maximum air velocity in this region will be $u \approx 53.5$ m/s, which is less than the speed of sound in air (340 m/s at $T = 20^\circ\text{C}$). Given these results it is relevant to presume that the Mach number, Ma is less than or equal (\leq) to 0.2, so the incompressible Navier-Stokes equations can be used for further simulations.

To estimate Reynolds number, both inlet parameters and parameters at the vocal cord gap are used to indicate what flow regime to expect. Velocities and diameters are taken from calculations above, and the kinematic viscosity of air is also used.

Using the above inlet parameters, the Reynolds number becomes $Re = \frac{Du}{\nu} \approx 7661$. If the parameters at the vocal cord gap are used, a Reynolds number equal to 22091 is obtained.

The critical Reynolds number for a transition from laminar to turbulent flow is not known for larynx. However, for flow in a pipe, the flow is assumed to be laminar until it reaches 2100, and turbulent from 4000 [28]. A turbulent flow regime is therefore assumed for further calculations with the simplified geometry in model 2.

6.2.2 Model 3 - real geometry

Even though the CT model, model 3, is more complex than the simple geometry used for comparison with the earlier thesis, the inlet of the throat is still assumed to be cylindrical, with a radius equal to 0.03 m. The inlet velocity becomes $u = 0.5896$ m/s, and the Reynolds number becomes $Re \approx 2319$.

The calculated Reynolds number is in the range of a critical Reynolds number for a pipe, hence a transitional flow regime is assumed for the simulations of model 3.

6.2.3 Calculation of the required number of steps

The number of steps needed in simulation to describe the situation occurring when laryngeal obstruction kicks in can be calculated from the equation

$$Number\ of\ steps = \frac{t^{period}}{timestep}, \quad (6.2)$$

where the size of the time step is 0.0005 sec. The time period of each inspiration is given by

$$t^{period} = \frac{\sum Volume_{lungs}}{\sum Volume\ flow_{inspiration}} = \frac{\sum V_{lungs}}{\sum Q_{inspiration}} \quad (6.3)$$

According to literature [41] the inspiratory capacity is equal to 3.5 litres for men and 2.4 litres for women, representing an average inspiratory capacity equal to 2.95 litres. No volume impact of age is assumed. Still assuming uniform volume flow, the inspiratory period becomes

$$t^{period} = \frac{2.95\text{litres}}{100\text{l/min}} = 1.77\text{s}, \quad (6.4)$$

and the number of steps becomes

$$Number\ of\ steps = \frac{1.77\text{s}}{0.0005\text{s}} = 3540. \quad (6.5)$$

6.3 Pressure drop

A pressure drop boundary condition is beneficial to include in the simulation models in order to maintain the numerical stability. This is of specific relevance in simulations involving fluid-structure interactions, as the pressure drop usually appears as the main driver of the process [8]. Calculation of the pressure drop to be applied in the simulations was accomplished by use of a reference simulation for each of the models. Based on an assumption

of a constant flow rate equal to 100 l/min, a calculated velocity was used as boundary condition for model 2 and model 3. A surface average simulation report was created for the inlet and outlet boundaries and an expression was created, where the inlet report was subtracted from the outlet report. The pressure drop was calculated for simulation model 1.0, model 2 and model 3.

6.4 Description of mesh

When a geometry is specified, grid points can be assigned and a mesh for the entire flow field can be developed. A mesh of the entire flow field is required for the solution to be able to march in space and time, so the discretized equations can be solved [27]. Several mesh characteristics exist as basis to achieve a favourable division of the geometry.

In this thesis, the surface remesher, polyhedral mesher, prism layer mesher, tetrahedral mesher and the thin mesher are used to obtain a suitable mesh for the models applied. The characteristics of the selected meshing models, taken from [31], are listed below:

- **Surface remesher:** Used to improve the overall quality of a surface. The surface is re-triangulated, which is favourable for optimization of the volume mesh models.
- **Polyhedral mesher:** Composed of polyhedral-shaped cells. Provides a balanced solution for complex mesh generation problems. Consists of cells, which are relatively easy to build, due to the fact that the mesh usually contains five times fewer cells than a tetrahedral mesh for a given starting surface.
- **Prism layer mesher:** Prismatic cells added next to wall surfaces and boundaries. Necessary to improve the accuracy of the flow solution, especially near walls and boundaries.
- **Tetrahedral mesher:** Provide an efficient and simple solution for complex mesh problems. Additionally, it is the fastest meshing model, using the least amount of memory for a given number of cells.
- **Thin mesher:** Prismatic layered volume mesh generated for thin geometries. Suitable for both simple and complex problems, and is efficient to produce a high quality grid.

6.4.1 Model 1 - validation

Model 1.0

The meshing models used for the simplified 2D-model are the surface remesher, polyhedral mesher and the prism layer mesher. The base size is set to 0.00102 m with a minimum surface size equal to 0.000454 m, posing a mesh consisting of 4261 cells. The mesh for model 1.0 is illustrated in figure 6.8a.

Model 1.1

The second 2D-model used for validation comprises meshing models like surface remesher, polyhedral mesher and prism layer mesher. The base size is set to 0.00102 m with a minimum surface size equal to 0.000454 m, creating a total of 4748 cells in the volume mesh. The mesh for model 1.1 is, shown in figure 6.8b.

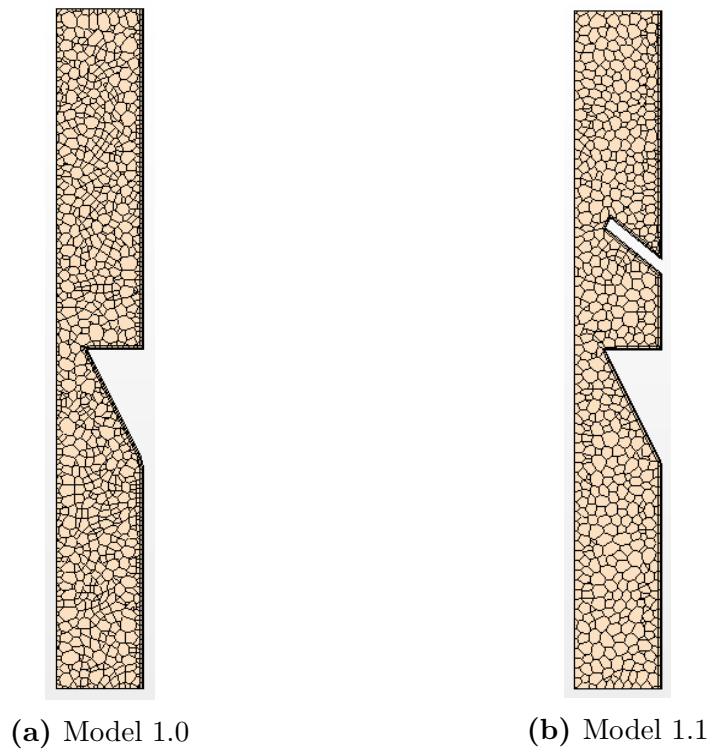


Figure 6.8: Mesh scene for model 1.

6.4.2 Model 2 - fluid-structure interaction

The models used to create a fluid mesh are the surface remesher, polyhedral mesher and prism layer mesher. The base size of the mesh is set to 0.0005 m, with a minimum surface size equal to 0.00005 m, so that the total number of cells in the fluid region is equal to 76717.

A finer mesh is necessary to obtain accurate simulations in the region where the interaction between the fluid and the solid occurs. Hence, a volumetric refinement is used to create a finer mesh comprising surface remesher, prism layer mesher and polyhedral mesher within the rectangle. The absolute size of this mesh is set to 0.00015 m.

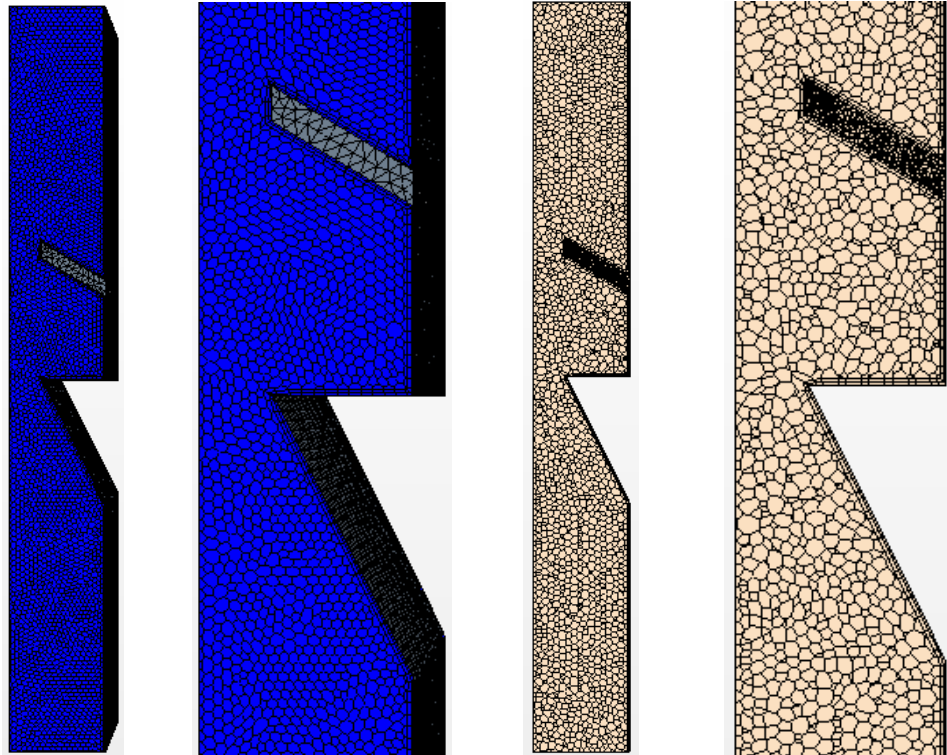


Figure 6.9: Mesh scenes for model 2. Volume mesh shown on left hand side, while right hand side displays surface mesh scenes.

The solid mesh consists of surface remesher, tetrahedral mesher and thin mesher. The base size is set to 0.001 m, with a minimum surface size equal to 0.0001 m. A total of 4376 cells constitutes the solid region.

An imprint operation is also implemented in order to trace the fluid and solid

parts. It is assigned a tolerance equal to 0.0001 m, and the merge/imprint method is set to discrete imprint surfaces. The resulting mesh type is conformal.

This results in a volume mesh consisting of a total of 81093 cells, shown at the left hand side of figure 6.9. The surface mesh scene is displayed at the right hand side in the figure.

6.4.3 Model 3 - real geometry

Model 3.0

The meshing models used for model 3 are the surface remesher, polyhedral mesher and the prism layer mesher. The base size is set to 0.001 m with an absolute size of prism layer thickness equal to 0.00033 m. This constitutes a mesh consisting of 2010700 cells, illustrated as a volume mesh in figure 6.10a. The surface mesh of the model is shown in figure 6.10b.

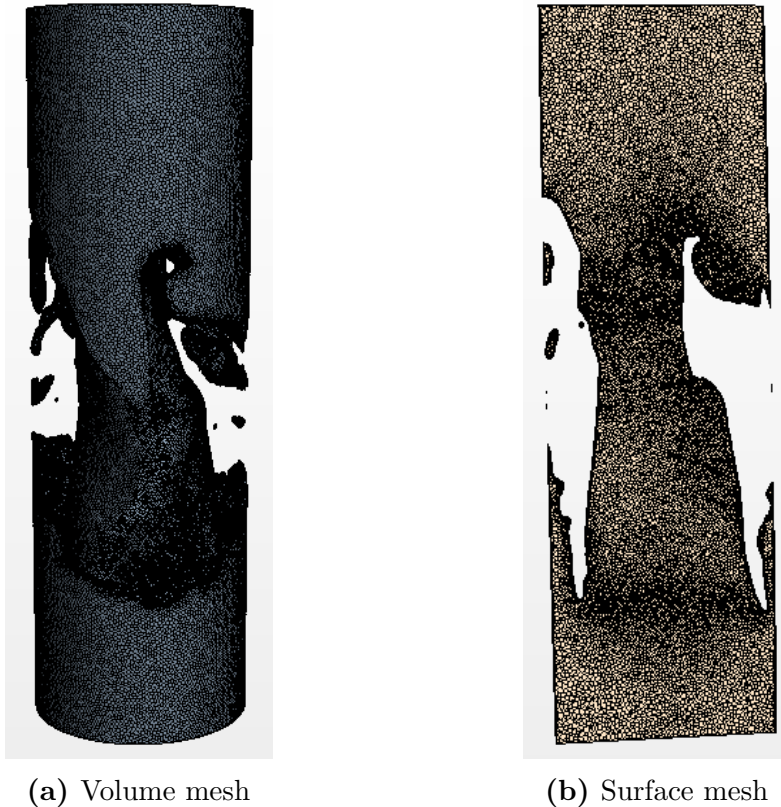


Figure 6.10: Mesh scene for model 3.0.

Model 3.1

The models used to create a fluid mesh are the trimmed cell mesher and the prism layer mesher. The base size of the mesh is set to 0.003 m, with a the size of the prism layer total set to 0.00099 m. The fluid region constitutes a total of 1157341 cells.

The solid mesh consists of surface remesher, tetrahedral mesher and thin mesher. The base size is set to 0.03 m, with a minimum surface size equal to 0.0045 m. The total number of cells in the solid region is equal to 4819.

An imprint operation is also implemented in order to trace the fluid and solid parts. It is assigned a tolerance equal to 0.0001 m, and the merge/imprint method is set to discrete impart surfaces. The resulting mesh type is conformal.

These three meshing operations results in a volume mesh comprising a total of 1162160 cells. The volume mesh scene is illustrated in figure 6.11a while figure 6.11b shows the surface mesh scene.

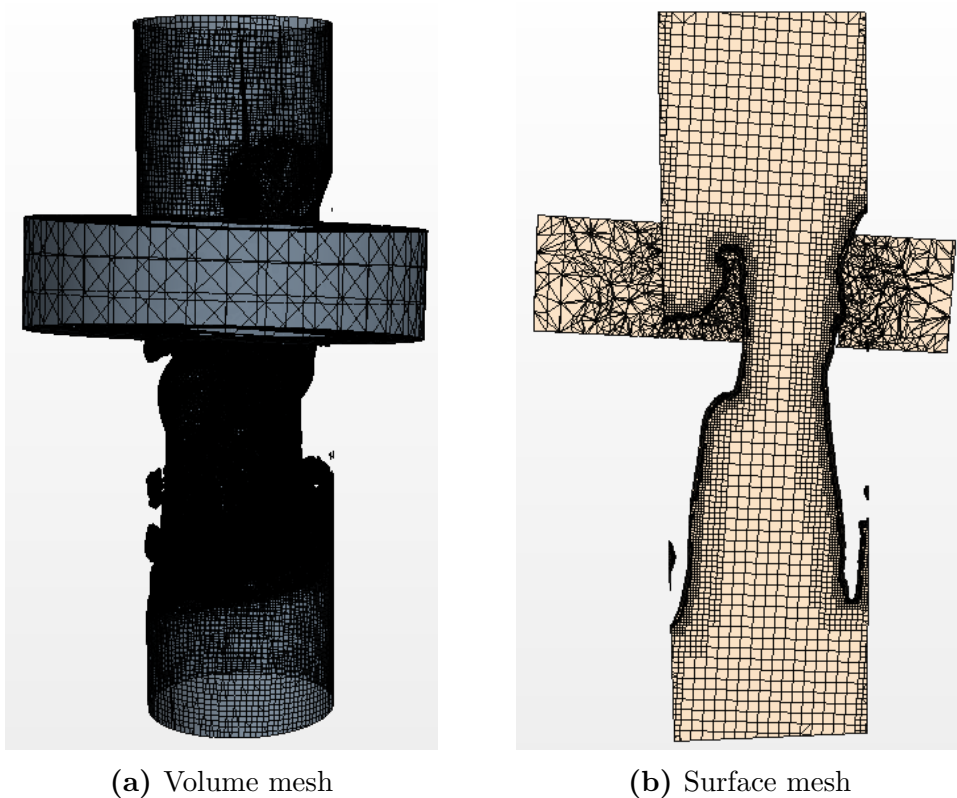


Figure 6.11: Mesh scene for model 3.1.

6.5 Selected simulation models

The primary variables in the simulation and the mathematical formulations used to generate a solution are defined through the selection of models. Their main purpose is to provide the solvers with the required equations and to collaborate with them to obtain a solution.

The following section presents the models used in this thesis and is based on the description given in the STAR-CCM+ user manual [31].

6.5.1 Fluid

Three dimensional, gas and constant density models

The three-dimensional model is designed to work on three-dimensional meshes, and is applicable when a three-dimensional mesh is desired. The gas model defines the equation of state for the density of the gaseous phase, meaning air in this thesis.

The density of the gaseous phase is assumed to be invariant throughout the domain, meaning that the density will not vary with temperature and the reference pressure will not have any impact on the calculations when the constant density model is activated.

Segregated flow, gradients and implicit unsteady models

The segregated flow model are used for incompressible or mildly compressible flows when computational resources are an issue. Thus, this implies that the model is normally used when the Mach number, $Ma \leq 0.2$.

The Gradients model is automatically selected once the space model, i.e. the segregated flow model, is defined.

The implicit unsteady model is the only unsteady model available with the segregated flow and segregated fluid energy models. When activated, objects that offer a choice between iteration or time-step for a trigger can be set to update at each time-step.

Turbulent, Reynolds-averaged Navier-Stokes and κ - ω turbulence models

The turbulent model is activated for situations with a turbulent flow regime. The selection of a turbulent flow regime will automatically select turbulence models that provide closure of Reynolds-averaged Navier-Stokes equations as a turbulence modelling approach.

The activation of the Reynolds-averaged Navier-Stokes turbulence model provide closure relations for the Reynolds-averaged Navier-Stokes equations to solve for the transport of mean flow quantities, as described previously in section 5.1.

The κ - ω turbulence model allows the computation of turbulent kinetic energy, κ and specific dissipation rate, ω , used to determine turbulent viscosity. These equations provide closure to the Reynolds-averaged Navier-Stokes equations, as described previously in section 5.1.1.

SST (Menter) κ - ω , All y^+ wall treatment and Exact wall distance models

Menter's SST K-omega model uses the insensitivity to free-stream conditions of the κ - ϵ model in the field far from the walls, while retaining the advantages of the κ - ω model near walls.

An accurate prediction of flow and turbulence parameters across the wall boundary layer is essential in most problems of practical importance due to the frequent vorticity in the flow near the walls. The all y^+ wall treatment combines the low- y^+ wall treatment for fine meshes with the high- y^+ wall treatment for coarse meshes.

The Exact wall distance model represents the distance from a cell centroid to the nearest wall face with a no-slip boundary condition. The model calculates an exact projection in real space, based on a triangular of the surface mesh. Various physical models require this parameter to account for near-wall effects, so the model is often selected automatically when a physical model that requires the wall distance parameter is selected. The physical model that requires exact wall distance in this thesis is the κ - ω turbulence model.

Cell quality remediation model

The Cell quality remediation model helps to identify poor-quality cells, and thereby contributes to solve mesh of poor quality. The computed gradients in the cells are modified once the cells are marked, and contributes to improve the strength of the solution.

As the solid stress model depends on the quality of the grid, activation of the Cell quality remediation model is recommended for solid stress analysis. The effect of improvement are generally only local to the poor cells, so the influence on the accuracy of the overall solution is small. However, the mesh quality metrics that marks the poor-quality cells are recomputed each time the mesh changes, so that the computational cost may increase for situations with moving mesh.

6.5.2 Solid

Three dimensional, Solid and Implicit unsteady models

The description in section 6.5.1 is applicable for both the Three dimensional model and the Implicit unsteady model.

The Solid model manages a pure substance in the solid phase, and should be activated when a single material solid part is to be modelled.

Solid stress and Linear isotropic elastic models

The Solid stress model computes the displacement of the solid structure under loads using the finite element method. The models is required for all types of stress analysis, as the corresponding stresses and strains are calculated throughout the displacement.

The Linear isotropic elastic model works with the Solid stress model in STAR-CCM+ and is automatically activated when the Solid stress model is chosen. The Linear isotropic elastic model accounts for the solid stress material, as the model establish a linear relation between stress and strain. STAR-CCM+ only supports linear elastic materials.

Fluid structure coupling

The Fluid structure coupling model are applicable for both one-way and two-way fluid-structure interaction simulations. The model is needed to allow for implicit coupling at the fluid-solid interface, and for motion models to account for the deformation of the fluid and solid meshes.

6.6 Solvers

In STAR-CCM+, the solution is controlled by solvers being activated once per iteration. The models described previously will select one or several required solvers in order to obtain a solution. A brief description of the solvers used in this thesis follows, based on a the description given in the user manual [31].

Segregated flow and implicit unsteady solver

The Segregated flow solver controls the solution update for the Segregated flow model. Additionally it controls the Velocity solver and the Pressure solver. The discretized momentum equation are solved by the Velocity solver to obtain the intermediate velocity field, while the Pressure solver solves the discrete equation for pressure correction and updates the pressure field.

The Implicit unsteady solver is used by the Implicit unsteady model, with a primary function of controlling the update at each physical time for the calculation. Additionally, it controls the size of the time-step.

Mesh morpher and solid stress solver

The Mesh morpher solver controls the calculations of morphing motion with specialized properties. Is it activated when the Morphing motion is selected for a region.

The Solid stress solver makes it possible to control different computation parameters such as verbosity, solver frozen and integration method. The solver also makes the estimation of the required simulation memory possible.

Fluid structure coupling and partitioning solver

The Fluid structure coupling solver works with the Fluid structure coupling model, and allows motion of models to account for the deformation of the fluid and solid meshes.

The Partitioning solver is responsible for controlling domain decomposition for parallel simulations, to ensure that the domain decomposition is up-to-date. This solver represents the partitioning approach for the simulation of a fluid structure interaction problem. The partitioned approach preserves software modularity because an existing flow solver and structural solver are coupled.

Wall distance and κ - ω turbulence and κ - ω turbulent viscosity solver

The Wall distance solver is used to calculate the Wall distance model. It becomes available when turbulence models are activated. The wall distance calculation takes place during the initialization step of the simulation.

The κ - ω turbulence solver and the κ - ω turbulent viscosity solver solve the κ - ω turbulence model as described earlier. The κ - ω turbulence solver controls the solution of the turbulence transport equations in all the continua for which a κ - ω is activated. The κ - ω turbulent viscosity solver controls the update of the turbulent viscosity.

6.7 Additional essential parameters

Additional essential parameters are specified in the following subsection.

Time step and inner iterations

The time step is set to 0.2 ms for model 1.0 and model 1.1 with temporal discretization set as first order. For model 2 the time step is 0.5 ms and the temporal discretization is set to second order. The time step for model 3.0 and 3.1 is set to 0.5 ms, and temporal discretization is set to first order. Transient simulations require discretization in time as well as space. When the temporal discretization is set to second order, the unsteady term uses the solution at the current time level, as well as those from the previous time steps to solve the equations [31].

The inner iterations are set to maximum 20 iterations per-one time step.

Under-relaxation factor

The under-relaxation factor (URF) decides how quickly the solver will obtain a solution for a particular simulation. The solution of the equation should, at each inner iteration, approach a value close to that of the previous inner iteration. A change in one variable affects the variables in the other equations, so the variation within each iteration can become large for complex problems, leading to unstable solutions. Under-relaxation factors are applied to yield a stable solution within each outer iteration. A part of a value from the previous iteration, equivalent to the URF-factor, are taken to dampen the oscillating behaviour of the solution for the current iteration. The factor differs from 0.0 to 1.0, where 1.0 denotes a solution without URF-factor. When URF are applied to a solver, the computational time of the specific problem will increase [27].

The κ - ω turbulence solver is assigned an URF-factor equal to 0.8 (default value), while a factor equal to 1.0 (default value) is assigned for the κ - ω turbulent viscosity solver throughout this study. Default values are also chosen as URF for the segregated flow solver, i.e. the URF for velocity is equal to 0.8, while the pressure is assigned an URF equal to 0.2.

6.8 Applied boundary conditions

Boundary conditions are applied to specify conditions on the solution domain boundary, in order to complete the mathematical models for the specific case. Boundary conditions are used on the faces that coincide with the boundaries of the computational domain [31]. The values that are not mentioned in this section are assigned default setting values.

The following parameters were set at the boundaries:

6.8.1 Model 1 - validation

Table 6.1: Boundary conditions for model 1

Part	Boundary conditions	Physics conditions	Magnitude
Inlet	Velocity inlet	Velocity specification	-4.855 m/s (y-direction)
		Turbulence specification	κ - ω
Outlet	Pressure outlet	Pressure	0 Pa
		Turbulence specification	κ - ω

The left hand side, the "front" and the "back" of model 1 were assigned the symmetry boundary condition. The remaining parts were set as walls, with the no-slip method assigned as shear stress specification.

The velocity component was iterated through a surface average velocity plot placed in the narrowest part of the model 1.0. Various inlet velocities were tried until a velocity equal to 14 m/s was obtained in the narrowest cross-sectional area. A velocity equal to 14 m/s was chosen due to the fact that Lacis [7] calculated this velocity in the narrowest part. With similar geometries and inlet velocities, a validation of the simplified models, model 1.0 and model 1.1 was possible.

6.8.2 Model 2 - fluid-structure interaction

Table 6.2: Boundary conditions for model 2

Part	Boundary conditions	Physics conditions	Magnitude
Fluid part		Motion Specification	Morphing
Inlet	Pressure outlet	Pressure	0 Pa
		Turbulence specification	κ - ω
Outlet	Pressure outlet	Pressure	-305.74 Pa
		Turbulence specification	κ - ω
Fluid/Solid contact	Mapped Contact Boundary	Morpher Displacement Specification	Solid stress
		Morpher Displacement	Displacement
Solid part		Motion Specification	Solid Displacement
		Mid-side Vertex Option	Add-Linear Interpolation
Fluid/Solid contact Segments	Mapped Contact Boundary Bottom	Constraint	Fixed
Fluid/Solid interface			
Fluid/Solid interface	Mapped Contact Interface	Topology	Indirect
		FSI Added Mass Control Option	Manual

The left hand side, the "front" and the "back" of model 2 were assigned the symmetry boundary condition. The remaining parts were set as walls, with the no-slip method assigned as shear stress specification.

The pressure drop was calculated as explained in section 6.3. When interfaces are assigned as mapped contact interfaces, data mapping between the finite volume (FV) and finite element (FE) meshes are allowed.

6.8.3 Model 3 - real geometry

Model 3.0

Table 6.3: Boundary conditions for model 3.0

Part	Boundary conditions	Physics conditions	Magnitude
Inlet	Velocity inlet	Velocity specification	-0.5896 m/s (z-direction)
		Turbulence specification	κ - ω
Outlet	Pressure outlet	Pressure	0 Pa
		Turbulence specification	κ - ω

Calculation of the inlet velocity is based on calculations in section 6.2.

The remaining parts were set as walls, with the no-slip method assigned as shear stress specification.

Model 3.1

Table 6.4: Boundary conditions for model 3.1

Part	Boundary conditions	Physics conditions	Magnitude
Fluid part			
Inlet	Pressure outlet	Motion Specification Pressure Turbulence specification	Morphing 0 κ - ω
Outlet	Pressure outlet	Backflow Specification Pressure Turbulence specification	Static -1.09 Pa κ - ω
Fluid/Solid contact	Mapped Contact Boundary	Backflow Specification Morpher Displacement Specification Morpher Specification	Static Solid Stress Displacement
Solid Part			
Fluid/Solid contact	Mapped Contact Boundary	Motion Specification Mid-side Vertex Option	Solid Displacement Add-linear Interpolation
Segments	Cylindrical edge	Constraint	Fixed
Fluid/Solid interface			
Fluid/Solid interface	Mapped Contact Interface	Topology FSI Added Mass Control Option	Indirect Manual

Calculation of pressure drop is based on calculations in section 6.3.

The interfaces are assigned as mapped contact interfaces to allow data mapping between the finite volume (FV) and finite element (FE) meshes.

The remaining parts were set as walls, with the no-slip method assigned as shear stress specification.

6.9 Mesh morphing

In fluid-structure interactions, the motion of the internal fluid vertices originates from the motion of the vertices on the solid surface. The morphing procedure, where the shape of the cells changes over time, but the neighbours

remain the same, is applied to deform these fluid vertices as a result of the deformations of the solid structure [31]. The Arbitrary-lagrangian-eulerian (ALE) method is used to solve the fluid transport equations. As described in section 5.2.4 the method accounts for the arbitrary motion of the mesh within the limit of moving boundaries. The redistribution of the vertices in the fluid mesh is defined by the movement of the prescribed structural solvers and their vectors, defined in section 6.6. The mesh morpher solver then uses this field to displace the actual fluid mesh vertices according to the displacements in the solid structure.

As each of the fluid boundaries interacts differently with the morphing procedure, a morpher node is assigned to each boundary. The interactions are dependent on how the mesh solver collects control vertices from the surface mesh [31]. The mesh morphers utilized in this study is solid stress and fixed:

- Fixed: the displacement associated with the vertices are zero, meaning that the boundary vertices are constrained and do not experience deformation
- Solid stress: the internal finite volume solid stress are utilized to calculate the displacements. In each time step, the vertices are taken from the underlying displacements calculated by the solid stress iterative solver.

7 Results and discussion

The following section includes results from simulations presented as snapshots illustrating velocity profiles and flow patterns. Several plots substantiating the results are also included. Following the results, some discussion around the subject matter is also comprised.

7.1 Validation of the simplified 2D-model

As the purpose of this thesis is to bring the results obtained from Lacis [7] a step further, there is a need to investigate and validate the simplified geometry used in model 1 in this study with [7]. To accommodate this, the geometrical model used by Lacis was reconstructed, with the parameters given in section 6.1 as basis.

7.1.1 Model 1.0

Lacis [7] figured out from calculations that the maximum velocity in his model was 14 m/s. A trial and error method (described in section 6.8.1) was carried out to find the appropriate inlet velocity to reproduce Lacis' result shown in figure 7.1a. An inlet velocity equal to 4.855 m/s was obtained in the negative y-direction. With a constant inlet velocity, the velocity field of the simplest 2D-model, model 1.0, was obtained as shown in figure 7.1b.

Considering pressure drop, Lacis [7] calculated it to be equal to 145.34 Pa, while simulations done as part of this study shows a pressure drop equal to 207.3 Pa. Thus, a difference equal to approximately 62 Pa was observed.

A possible explanation to the difference in pressure drop may be the variance in thickness between Lacis' model and model 1.0. Lacis' model was created in 2D, while a depth of 4 mm was selected for this study to give model 1.0 a 2D expression. Li et al. [26] suggest that intraglottal pressure distributions depend upon glottal shape, size and diameter. As the simulation model used in this study has a slightly greater surface area and volume than Lacis' model, it seems reasonable that a higher pressure drop was observed for model 1.0.

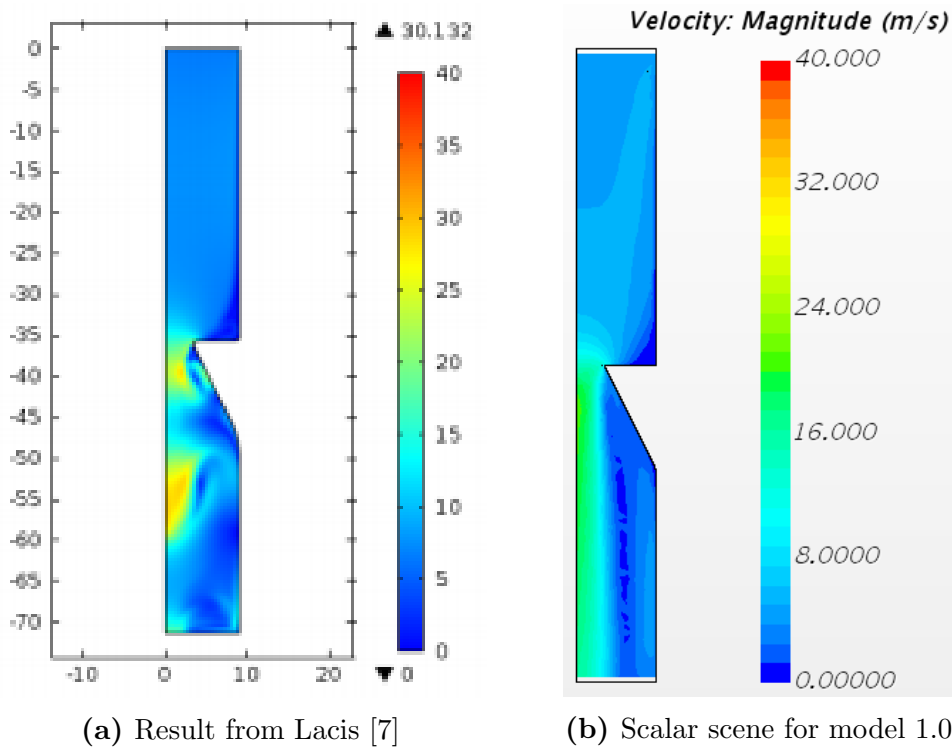


Figure 7.1: Comparison between Lacin [7] model for simplified geometry (left) and model 1.0 used in this study (right).

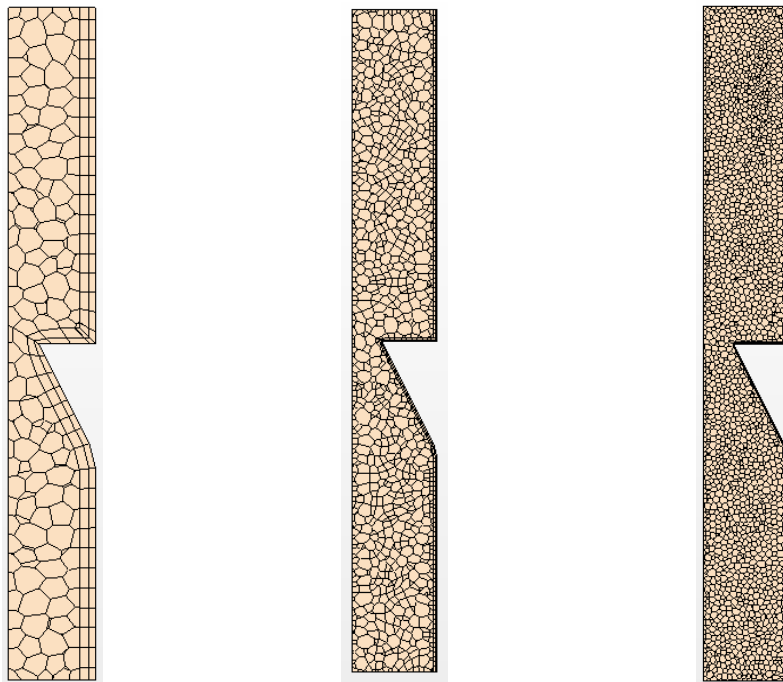
Comparing the velocity profiles in figure 7.1 there are not many striking similarities between Lacin’s model and model 1.0. However, the magnitude of velocity in the two models is of the same order in the area representing the narrowest part of the throat, i.e. the vocal cords. Additionally, it seems to be a good correlation between the inlet velocities in the two models compared. Even though the velocity magnitudes correspond to each other, the flow patterns differ, especially for the flow regime after the narrowing of the throat.

By careful inspection a distinction in the tip of the geometry supposed to represent the vocal cords can be recognized. Lacin [7] had a rounded tip on his vocal cord part, while no smoothing tool was used when constructing the simulation models in this thesis. As there is a difference in the sharpness of the tip, a difference in the separation point in the area near the vocal cords may be possible for Lacin’s model and model 1.0, respectively. The smoothed tip used by Lacin’s may explain the first swirl after the vocal cords in his model, but it does not explain the second swirl. However, this small inequality in geometry may represent a possible explanation to some of the

differences in the flow patterns, expressed in figure 7.1.

Sensitivity analysis for model 1.0

Other possible explanations to the difference in flow pattern and flow regime may relate to boundary conditions, number of steps, time step and the base size of the grid. In this thesis, the time step and the base size were suggested as explanatory parameters, and were thereby chosen for further assessment. Variation of the above parameters were tested to see how they affected the results in model 1.0 through a case study. Hence, an indication of the numerical stability of the simplified model was outlined.



(a) Base size = 0.005 m (b) Base size = 0.00102 m (c) Base size = 0.0005 m

Figure 7.2: Variation of the base size of the computational grid for model 1.0.

As shown in figure 7.2 the base size clearly affects the quality of the mesh. Figure 7.2a possess a total of 808 cells, figure 7.2b holds 4146 cells and figure 7.2c includes a total of 26626 cells. Generally, a more accurate solution is obtained when the base size of the computational grid is reduced. However, the solution time increases sufficiently, so a finer mesh is not always preferred.

The parameters given in 6.4.1 was chosen as basis for the validation of the model 1.0, in the same manner as Lacis [7] used in his simulations.

Figure 7.3 illustrates flow patterns corresponding to the different meshes shown in figure 7.2. Even though the flow patterns are mostly similar, inequalities can be seen in the region where the increased flow velocity occurred. A slight increase in the maximum velocity can be observed as the base size decreases. The finer the mesh, the higher becomes the maximum velocity, and the more prominent and clear becomes the flow pattern. All these parameters contribute to a more accurate solution, implying that the finest mesh provides the most confident solution. However, as the maximum velocity and the flow patterns in figure 7.3b and 7.3c are approximately the same, a base size equal to 0.00102 m is chosen to reduce the computational time, for the further investigation of model 1.0.

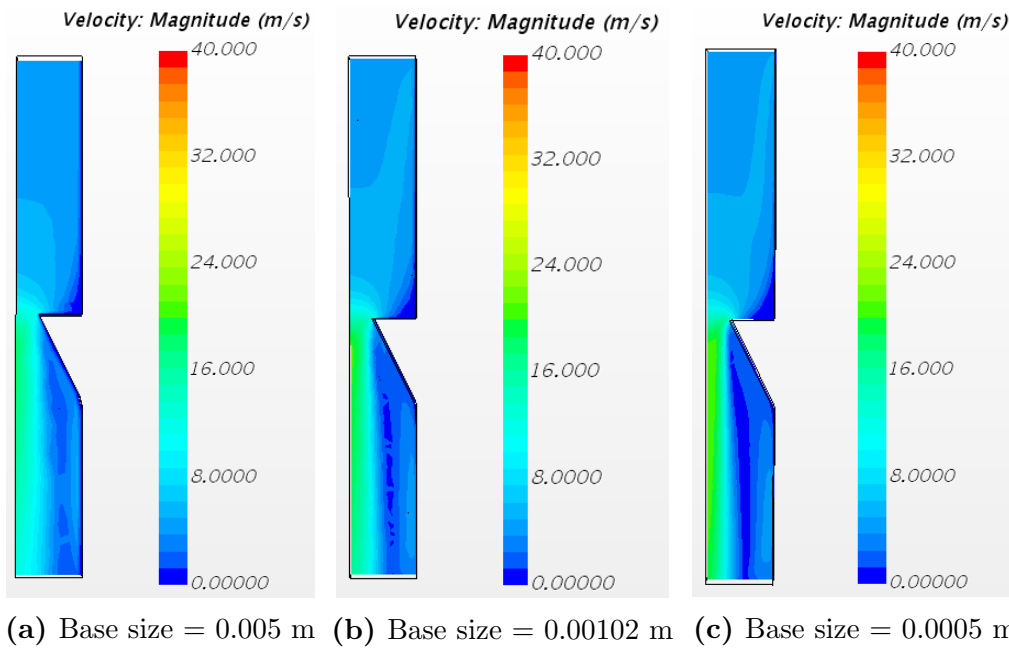


Figure 7.3: Influence of the varied base size of the computational grid on the flow pattern.

The time step plays an important role due to the stability of the solution. Hence, various values were tested. Lacis [7] numerically estimated a time step equal to 0.1-0.2 ms. Additionally, he estimated a value equal to 0.5 ms from a simple dimensional analysis. However, it is not clear what value he chose for the simulations in his study, but a time step equal to 0.2 ms was chosen as starting point in this study for simulation model 1.

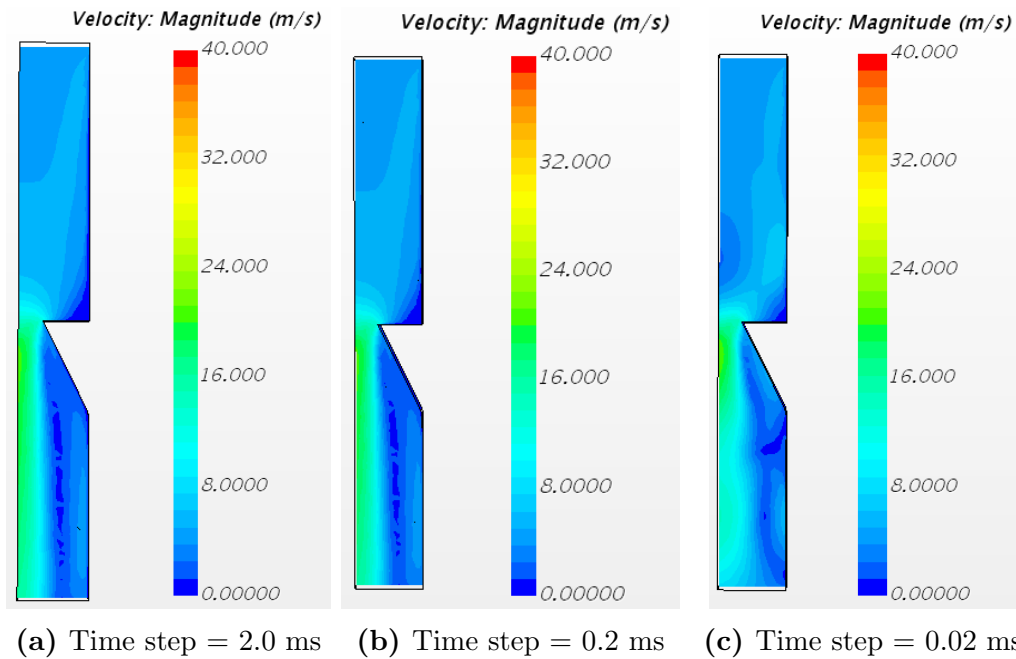


Figure 7.4: Influence of varied time step on the flow pattern.

The testing of different values of time step resulted in approximately equal velocity magnitudes. In addition, flow patterns were virtually equal. This is shown in 7.4. As the different time step values provide approximately equal velocities and flow patterns, the size of the time step is not critical for model 1.0. These findings support that the results obtained in this study for model 1.0 seems reasonable.

7.1.2 Model 1.1

The more realistic, but still simplified model, model 1.1, was investigated and compared with the studies carried out by Lacin [7]. A similar inlet velocity as for model 1.0 was assumed for model 1.1.

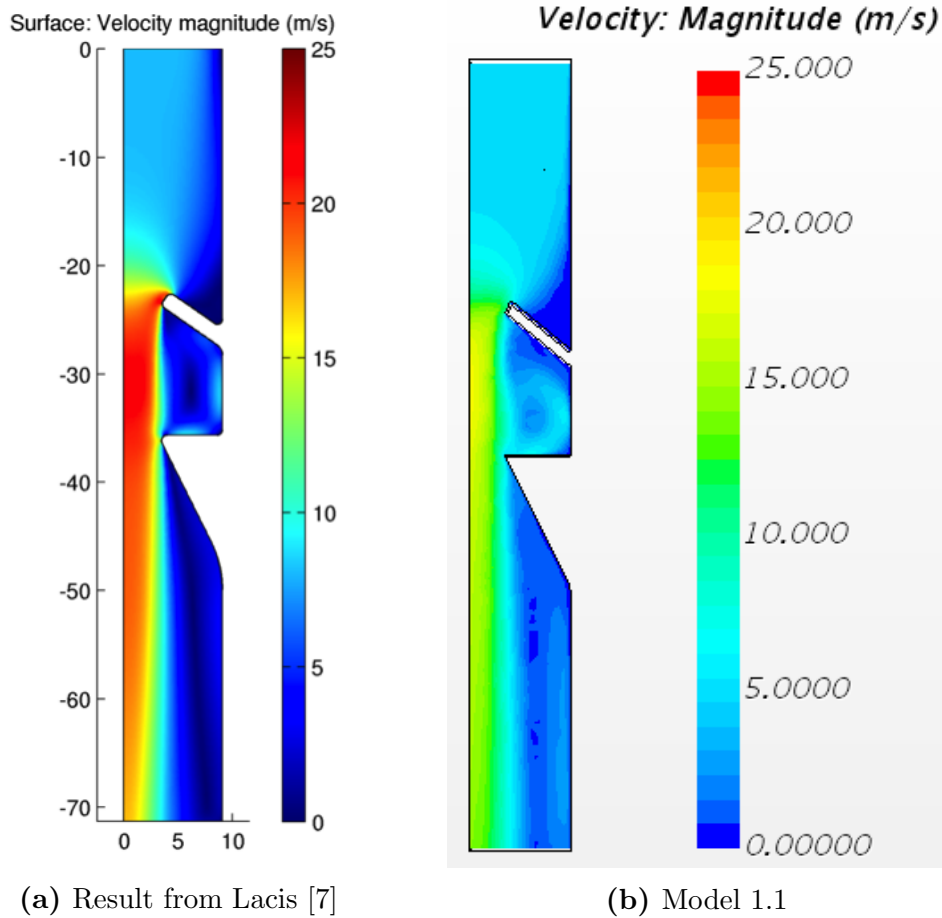


Figure 7.5: Corresponding flow pattern to model 1.1.

As Lacis [7] did not specify the corresponding pressure drop to figure 7.5a, an investigation of the pressure drop for simulation model 1.1 is also omitted in this study.

When comparing the maximum velocity and the flow patterns in figure 7.5, similarities are noted for the flow patterns and also for the velocity magnitude at the inlet. However, it is observed that the velocity magnitude in the epiglottic fold and the vocal cord area is significantly higher in Lacis model (figure 7.5a) than it is in model 1.1 (figure 7.5b) in this thesis. Nevertheless, for both situations, the velocity increases significantly when the flow passes the epiglottic fold.

As the development of velocity and the flow patterns are fairly similar for the models in figure 7.5, it can be stated that model 1.1 can be considered fairly valid when velocity and flow patterns are studied.

7.1.3 Overall assessment of the validity of model 1

The flow patterns in figure 7.1 and 7.5 are clearly affected throughout the laryngeal domain. This indicates the magnitude of impact obstacles, like the vocal cords and the epiglottic fold, have on the flow velocity in the domain. As a constant inlet velocity is applied as boundary condition for the model 1 simulations, the same amount of fluid will strive to pass through the domain regardless of geometrical configuration. Hence, a reduction in the cross-sectional area results in an increased flow velocity in agreement with continuity equation. At a higher velocity, the flow becomes more turbulent, i.e. the Reynolds number increases. Breathing becomes more difficult when size and number of eddies in the flow increase. It is thereby reasonable to state that the geometry and/or position of the vocal cords and the epiglottic fold, representing obstacles, plays an important role for the breathing process, when inlet velocity is the driver of the flow.

In summary, there is not one specific parameter that can explain the difference in flow patterns alone. Lacis' did not specify all the parameters applied in his thesis, making it difficult to correctly reproduce his model. A number of variables constitutes possible explanations, such as a slight difference in turbulence model applied, in addition to a possible difference in the numerical model chosen by the numerical simulation software to solve the problem. Other suggested explanations may be difference in simulation time, difference in simulation time-step and difference in boundary conditions applied to the model.

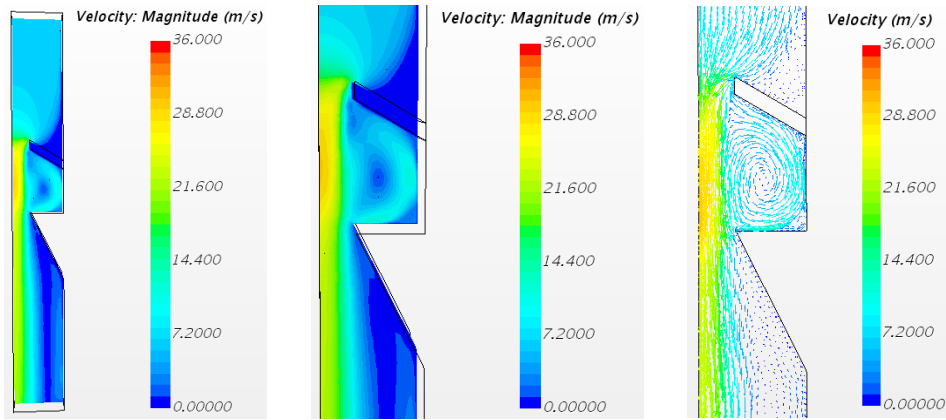
Even though the most simple simulation model 1.0 is not equal to the model obtained by Lacis [7], the resulting flow patterns for varied base size (figure 7.3) and varied time step (figure 7.4) support the results obtained in this thesis. A comparison between model 1.1 and Lacis [7] substantiates the assertion, through approximately similar flow patterns and a somewhat similar velocity magnitude. Based on this, a validation of the simplified models used in this thesis is accomplished.

7.2 Fluid-structure interaction on a simplified 3D-model

This section contains screenshots presenting flow patterns, in addition to plots for velocity, displacement and volume flow for various values for Young's modulus, E . Three values of E were chosen as most relevant; 0.45 MPa, 0.518 MPa and 3.33 MPa, forming the basis for the results to be presented. In the end of the section, unified plots are shown. Additional results for Young's

modulus equal to 0.8 MPa, 1.0 MPa, 2.0 MPa and 4.0 MPa are included in the unified plots. The unified plots illustrate how Young's modulus affects steady-state maximum velocity obtained in the domain, steady-state displacement of the epiglottic fold and steady-state volume flow at the outlet, i.e. the lungs, in the simplified 3D-model utilized in this study.

Firstly, a reference simulation with the epiglottic fold in a static position, and a calculated pressure drop equal to -305.74 Pa as the driver of the air flow, was conducted. The obtained flow patterns for the steady-state solution for the static situation are shown in figure 7.6. Figure 7.7a displays the plot for volume flow at the outlet for the steady-state situation, implying a stable volume flow equal to $0.0008 \text{ m}^3/\text{s}$. A steady-state maximum velocity equal to 29.7 m/s was observed in the fluid domain for the static situation, illustrated in figure 7.7b.



(a) Static total velocity (b) Static velocity scene (c) Static velocity vector

Figure 7.6: Flow patterns for steady-state velocity for model 2 with no movement in the epiglottic fold, i.e. a static situation. Assumed to be the starting point in all simulations.

The small oscillation in the beginning of figure 7.7a and figure 7.7b is assumed to be due to numerical instabilities, implying that the program needs some iterations before it becomes steady at a correct value according to simulations.

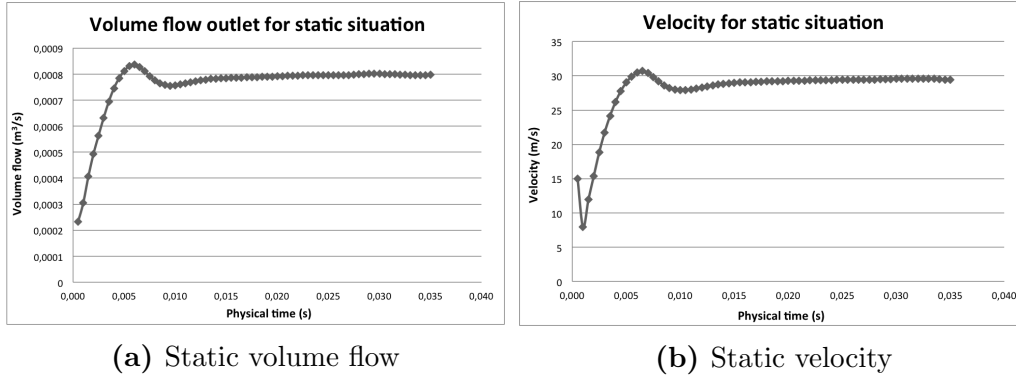


Figure 7.7: Volume flow at the outlet and velocity plot for a static situation in model 2.

Thereafter, seven different simulations were performed using fluid-structure interaction in model 2. The magnitude of Young’s modulus was varied for each of the simulations. A constant pressure drop equal to -305.74 Pa was assigned as outlet boundary condition for all simulations, acting as the driver of the fluid flow.

In the following, snapshots of flow patterns are shown for the three presented simulations, respectively E equal to 0.45 MPa, 0.518 MPa and 3.33 MPa. Accordingly, a plot describing displacement of the solid part as a function of physical time, and a plot describing volume flow at the outlet as a function of physical time were produced for each of the different cases. The displacement is given in mm, while the volume flow is given in m^3/s . As the fluid (air) propagates in the negative y -direction, the positive y -axis constitutes the absolute values for displacement and volume flow.

7.2.1 Results for E equal to 0.45 MPa

The lowest value for Young’s modulus approved for the model in STAR-CCM+ is found to be 0.45 MPa. The program stopped running for lower values for Young’s modulus for the assigned pressure drop. This can be explained by the occurrence of cells with zero or negative volume in the simulations. The simulated flow patterns for maximum velocity and steady-state maximum velocity are shown in figure 7.8. A corresponding displacement plot is shown in figure 7.9. A maximum displacement equal to 1.75 mm was observed for the epiglottic fold part, with a steady-state displacement equal to 0.56 mm. For the volume flow plot, illustrated in figure 7.10, a minimum

flow equal to $0.000147 \text{ m}^3/\text{s}$ was reached, and the volume flow became steady at $0.0005 \text{ m}^3/\text{s}$.

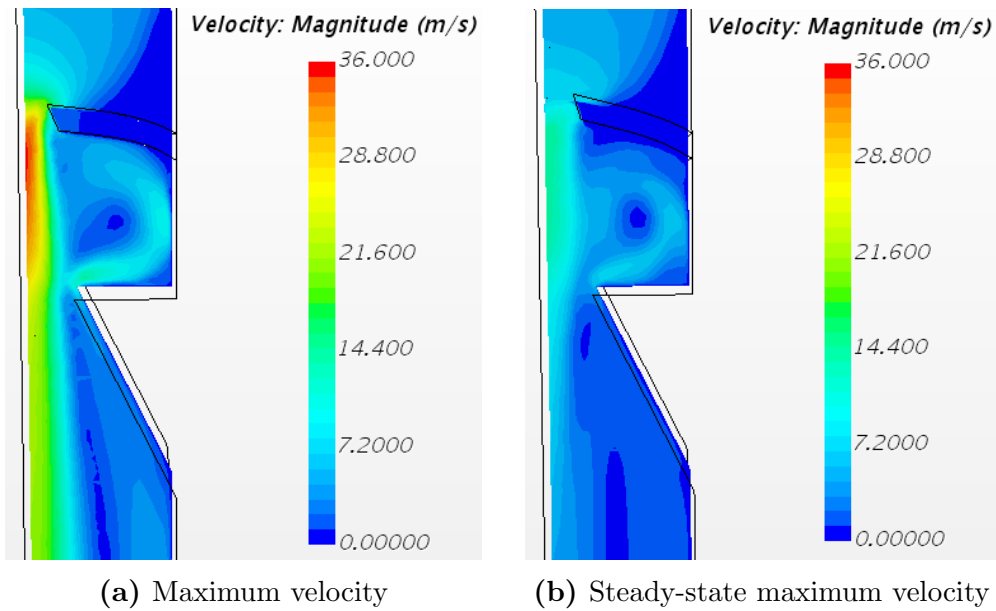


Figure 7.8: Flow patterns for maximum velocity and steady-state maximum velocity for $E = 0.45 \text{ MPa}$.

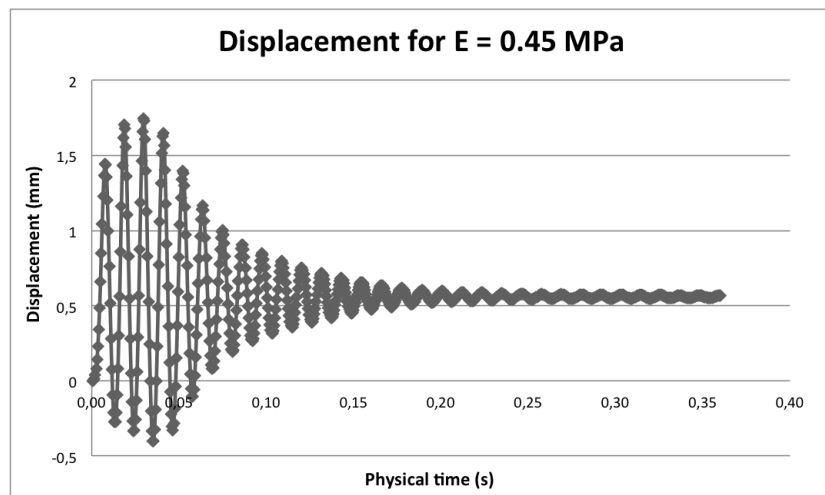


Figure 7.9: Displacement for $E = 0.45 \text{ MPa}$.

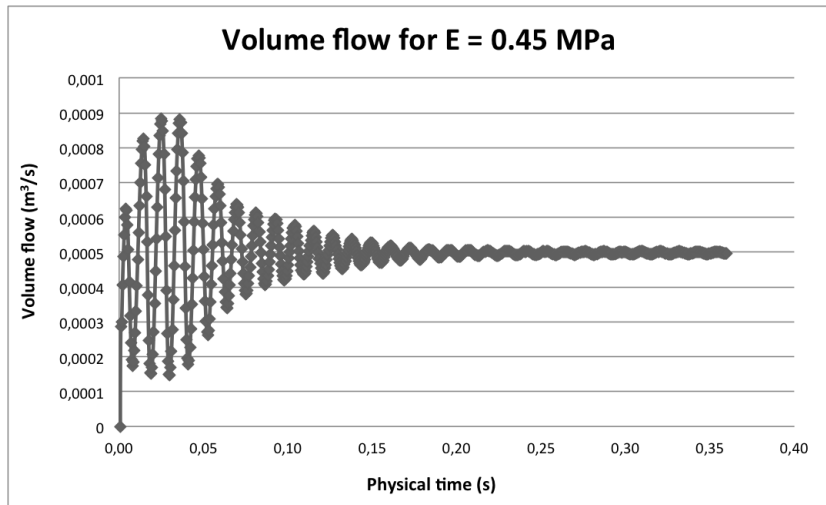


Figure 7.10: Volume flow at the outlet for $E = 0.45$ MPa.

7.2.2 Results for E equal to 0.518 MPa

The solid material with the least value for Young's modulus given in STAR-CCM+ is rubber with E equal to 0.518 MPa. A simulation was therefore performed for Young's modulus equal to this value. The simulated flow patterns for maximum velocity and steady-state maximum velocity are shown in figure 7.11. A corresponding displacement plot is shown in figure 7.12. A maximum displacement equal to 1.52 mm was observed for the epiglottic fold, with a steady-state displacement equal to 0.53 mm. For the volume flow plot, illustrated in figure 7.13, a minimum flow equal to $0.000187 \text{ m}^3/\text{s}$ was reached, and the volume flow became steady at $0.00056 \text{ m}^3/\text{s}$.

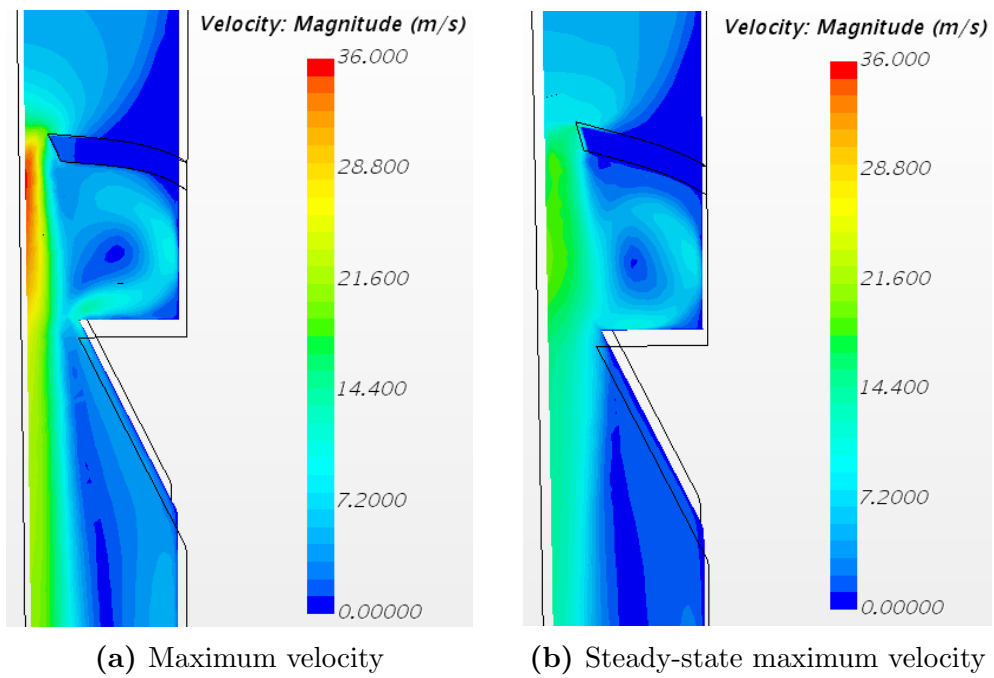


Figure 7.11: Flow patterns for maximum velocity and steady-state maximum velocity for $E = 0.518$ MPa.

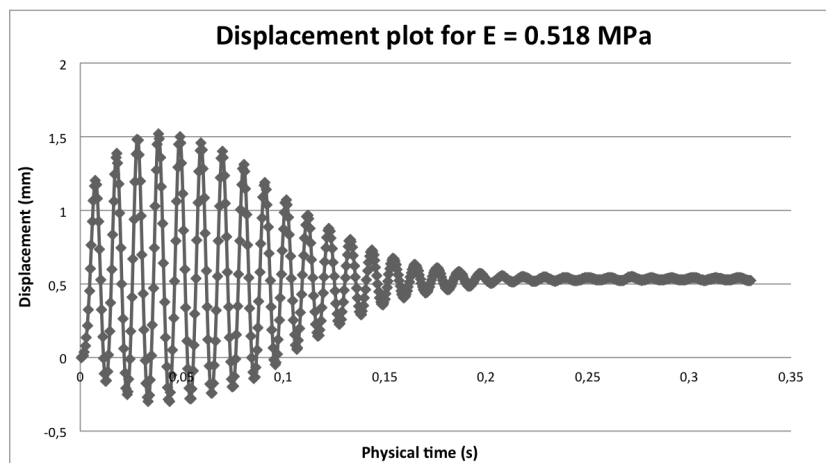


Figure 7.12: Displacement for $E = 0.518$ MPa.

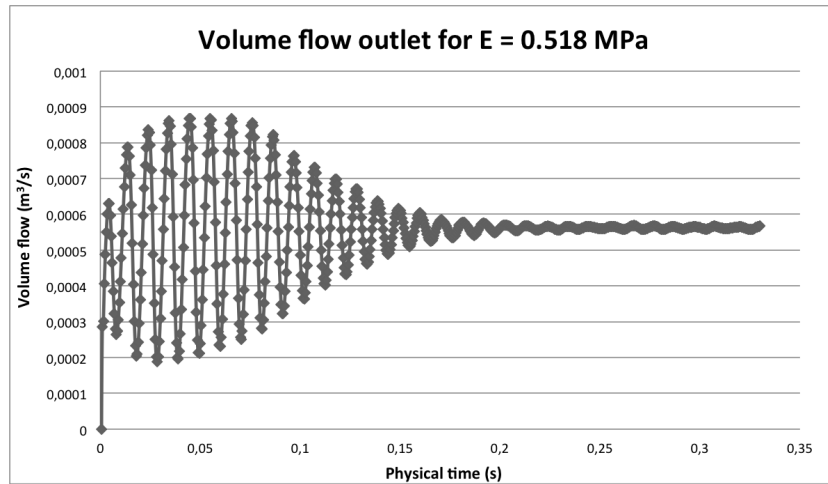


Figure 7.13: Volume flow at the outlet for $E = 0.518$ MPa.

7.2.3 Results for E equal to 3.33 MPa

According to Trabelsi [13], the value for Young's modulus for cartilage is equal to 3.33 MPa. As the cartilage constitutes the epiglottic fold (cuneiform cartilage), it is reasonable to believe that this will be the correct value for Young's modulus for a normal larynx. Simulated flow patterns for maximum velocity and steady-state maximum velocity are shown in figure 7.14. A corresponding displacement plot is shown in figure 7.15. A maximum displacement equal to 0.0996 mm was observed for the epiglottic fold, with a steady-state displacement equal to 0.083 mm. For the volume flow plot, illustrated in figure 7.16, a minimum flow equal to $0.00072 \text{ m}^3/\text{s}$ was reached, and the volume flow became steady at $0.00076 \text{ m}^3/\text{s}$.

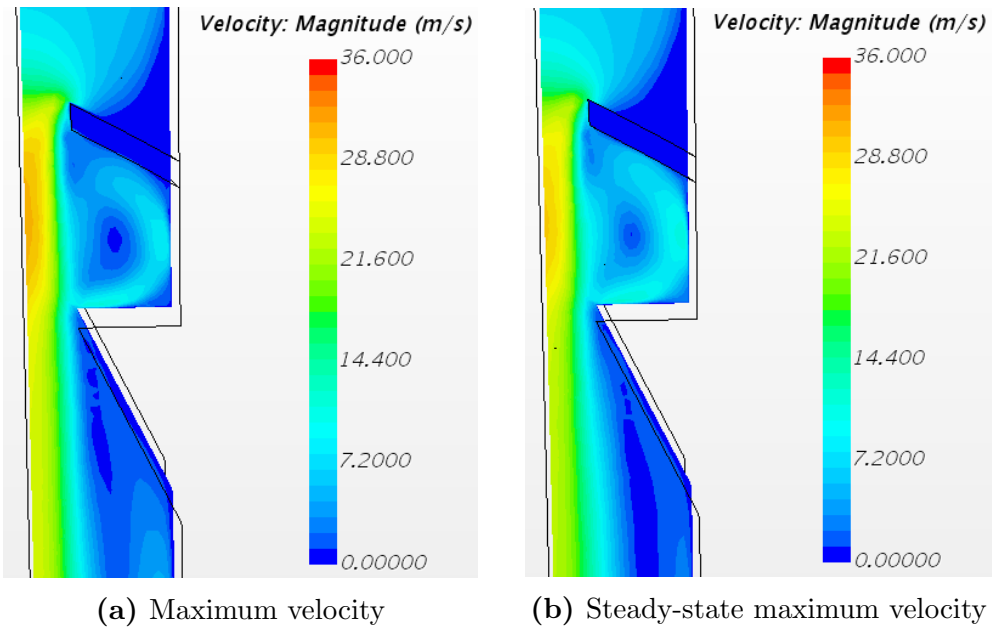


Figure 7.14: Flow patterns for maximum velocity and steady-state maximum velocity for $E = 3.33$ MPa.

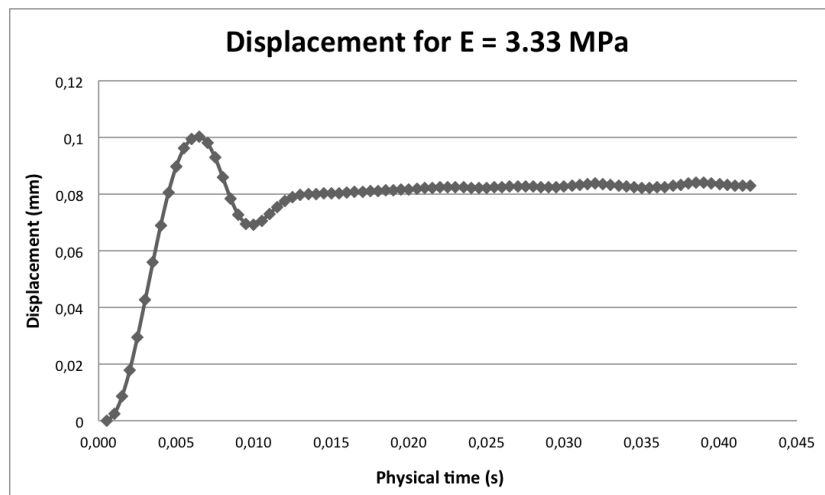


Figure 7.15: Displacement for $E = 3.33$ MPa.

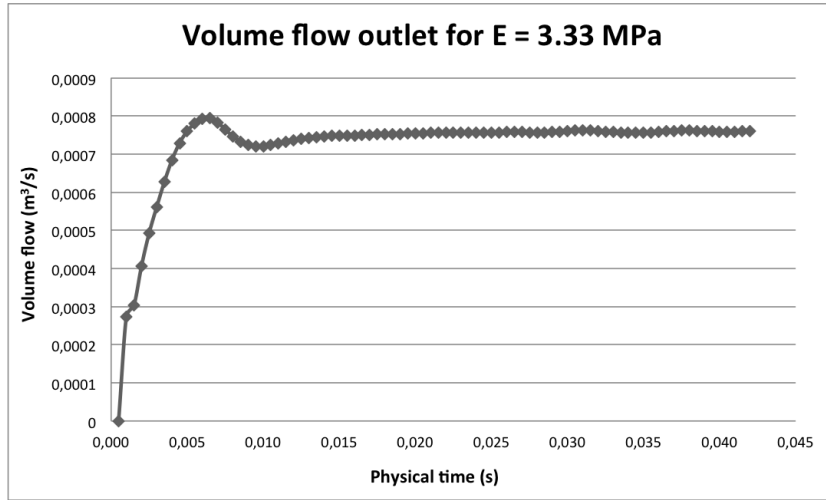


Figure 7.16: Volume flow at the outlet for $E = 3.33$ MPa.

The displacement of the epiglottic fold is slightly affected in a normal larynx during heavy exercise, which correlates well with the displacement plot shown in figure 7.15. The minor displacement observed in the plot explains the slight reduction in volume flow, as can be seen in figure 7.16. The slight reduction in volume flow may explain why every individual experience that breathing gets harder during heavy exercise, even with a normal larynx. Hence, the above presented plots support Trabelsi's studies suggesting that the value for Young's modulus for a cartilage in a normal larynx is equal to 3.33 MPa.

7.2.4 Preliminary summary for model 2

Fluctuations in displacement and volume flow occur in the beginning of the physical time in the displacement and volume flow plots presented. As noted earlier, numerical instabilities in the programme can explain such behavior. In fluid-structure interaction, the fluctuations indicate how the fluid forces and elastic forces interact until a steady-state solution is reached, i.e. fluid forces and elastic forces are approximately equal.

Generally, results from the presented plots for E equal to 0.45 MPa, 0.518 MPa and 3.33 MPa indicate that the displacement of the epiglottic fold and the volume flow at the outlet is inversely proportional, i.e. an increase in displacement causes a decrease in the volume flow.

As indicated, E equal to 3.33 MPa is assumed to represent a normal larynx. Hence, it seems reasonable that the simulated displacement and volume flow

plot related to E equal to 0.45 MPa (shown in figure 7.9 and figure 7.10) might represent the actual situation observed to arise for individuals affected by EILO. Comparing the steady-state values for volume flow at the outlet for a normal larynx ($0.00076 \text{ m}^3/\text{s}$) with an EILO larynx ($0.0005 \text{ m}^3/\text{s}$), a difference equal to 34 % is observed. Thus, there is a significantly smaller amount volume of air reaching the lungs during strenuous exercise for an EILO patient, compared to a person with a normal larynx.

Furthermore, a closer study of the development of the epiglottic fold displacement plots indicate how the displacement is affected as a function of physical time. Initially, the epiglottic fold is exposed to large displacements. However, it returns to its initial condition, before it is displaced again. The duration of this process varies for different values of Young's modulus. A common feature between the plots (especially figure 7.9 and figure 7.12) is a declining trend for both the displacement and the return of the epiglottic fold with physical time, until the fold becomes steady at a displaced point.

Such chain of events may remind of an assumed development of displacement of the epiglottic fold during strenuous exercise for individuals affected by EILO. For affected individuals, the displacement of the epiglottic fold increases with increased intensity (i.e. increased volume flow), until the epiglottic fold suddenly collapses after some time. Göçkan et al. [17] suggest that the aerodynamic properties of the larynx alter due to loss in muscular tonus (normal state of tension in a tissue). If this applies for an EILO larynx, it may indicate that the ability to resist changes decreases over time for the epiglottic fold. Such situation suggests that the fold becomes exhausted during strenuous exercise, and an obstruction thereby occurs when fatigue is reached. Despite this, it is difficult to state whether the obstruction is caused by exhaustion of the physical properties within the throat, or if it occurs due to an increased volume flow.

7.2.5 Velocity for E equal to 0.45 MPa, 0.518 MPa and 3.33 MPa

The next question of interest is how the displacement and volume flow does affect the maximum velocity obtained in the domain. Based on the figures presented in section 7.1 an increase in velocity should be expected in the region representing the epiglottic fold and the vocal cords.

Maximum velocity magnitude for the three different values of Young's modulus are plotted in figure 7.17. The different lines describe the development

of the maximum velocity throughout the simulation for each situation.

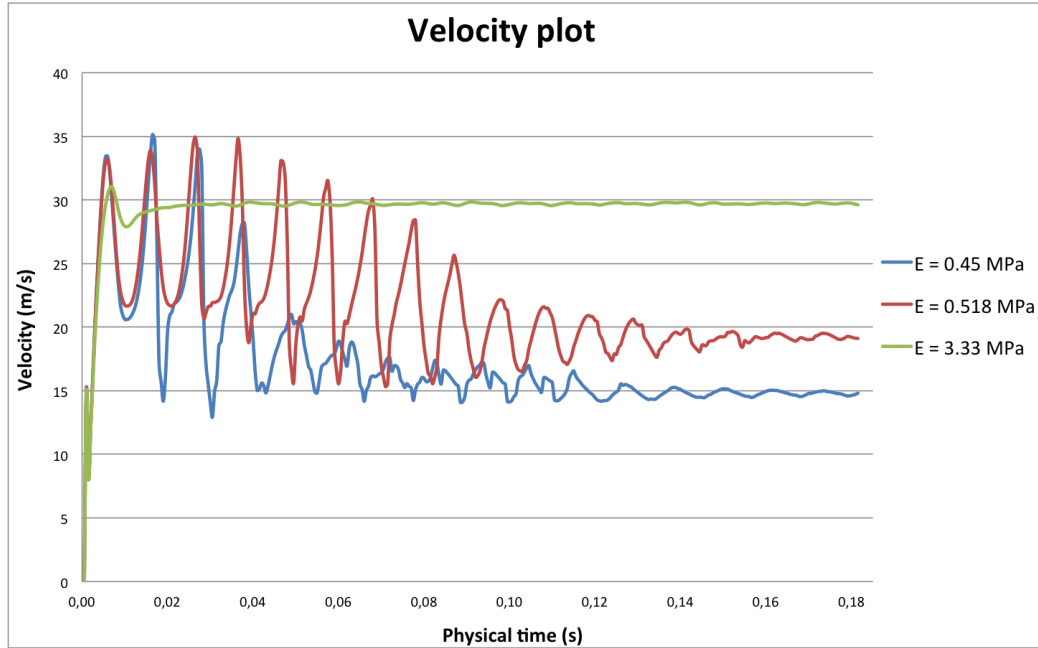


Figure 7.17: Maximum velocity obtained in the domain as a function of physical time for different values of Young's modulus.

It can be read from the plot in figure 7.17 that the steady-state maximum velocity becomes 14.8 m/s, 19.5 m/s and 29.7 m/s for values of E equal to 0.45 MPa, 0.518 MPa and 3.33 MPa, respectively. These observations implies that the steady-state maximum velocity magnitude increases with an increasing value for Young's modulus.

The large fluctuations in the beginning of the simulation time once again indicate how the fluid forces and the elastic forces in the domain interact until a steady-state solution is reached. Nevertheless, the duration of the big fluctuations implies that other factors seem to affect the velocity development. Additionally, an approximately constant frequency is noticed for the fluctuations in each of the simulations presented in the plot. This may indicate that turbulence effects should be considered as possible explanatory cause to the fluctuations. Comparing the fluctuation frequency for the three situations in the beginning of the plot (physical time 0-0.04 s), they seem to correlate well. In a turbulent flow, eddies are formed and constantly develop in a continuous cycle. Such effects affect the development of the flow and thereby also the maximum velocity in the domain. Thus, turbulence may

constitute a possible explanation to the big persisting fluctuations and the correlating frequency of the fluctuations, observed in the beginning of figure 7.17.

A scalar representation and a vector representation of the steady-state maximum velocity patterns obtained are presented in figure 7.18 and 7.19.

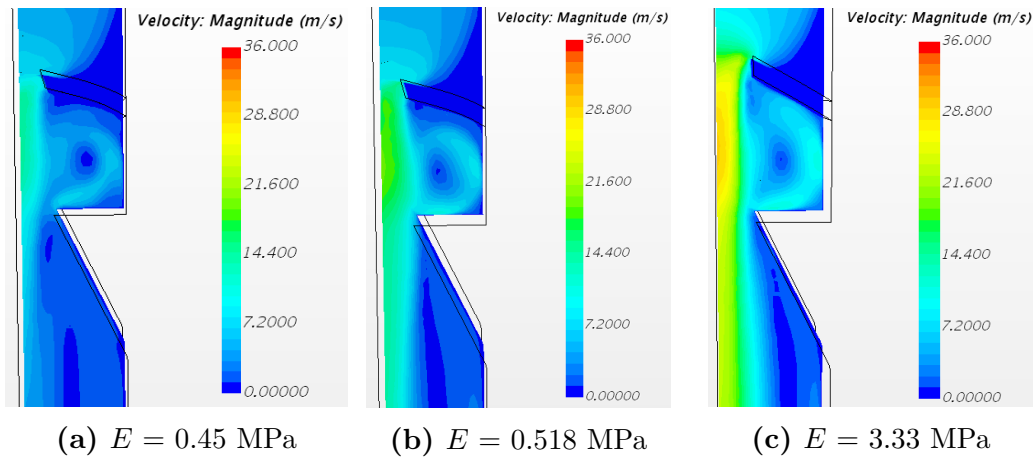


Figure 7.18: Scalar representations of the steady-state maximum velocities obtained for different values of E .

Generally, regardless of position of the epiglottic fold, figure 7.18 indicates an increase in velocity in the region representing the epiglottic fold and the vocal cords as suggested in the beginning of this section. However, the presented snapshots indicates a difference in size of increase in the velocity magnitude as the magnitude of E varies.

Figures 7.18 and 7.19 illustrate the increased velocity magnitude in the region between the epiglottic fold and the vocal cords. A general trend is that the velocity magnitude is reduced when the displacement increases, i.e. the Young's modulus decreases. As the pressure drop is constant and appears as the driver of the airflow, the steady-state velocity in the domain will decrease when the resistance increase. Since an increased displacement of the epiglottic fold involves an increased resistance, the obtained results correlate with the principles from the Bernoulli-equation.

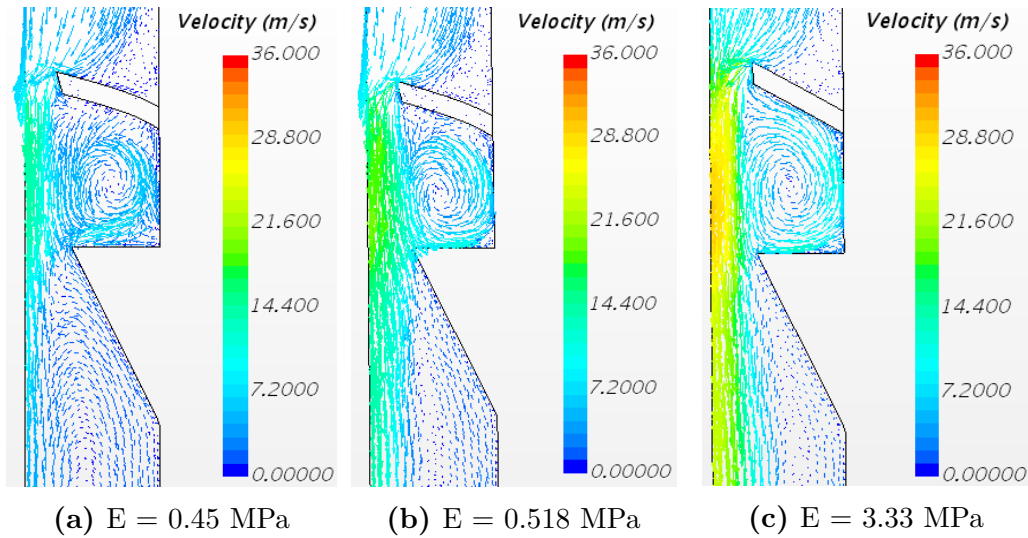


Figure 7.19: Vector representations of the steady-state maximum velocities obtained for different values of E .

A closer study of figure 7.19 indicates a difference in the vector field, especially in the region over the epiglottic fold and in the area between the epiglottic fold and the illustrated vocal cords. Comparing the vector scenes, the flow seems to be separated at different areas, indicating that the separation point is affected by the value of Young's modulus (resulting in different positions of the epiglottic fold). This implies a difference in separation point for flow based on different glottal angles. As a consequence, the vector scenes indicate an area of stagnation in the area between the epiglottic fold and the vocal cords. Hence, the results are in correlation with studies by Göçkan et al. [17], suggesting that a flow separation at glottis level will produce areas of stagnation in the subglottis and trachea during inspiration.

In summary, an increase in steady-state velocity in the region representing the epiglottic fold and the vocal cords occurred as presumed. However, the magnitude for Young's modulus seems to impact the size of the increase in velocity. Observations made based on figure 7.17 imply that the steady-state maximum velocity increases when Young's modulus increases, i.e. displacement of the epiglottic fold decreases. Figures 7.18 and 7.19 substantiate the observations.

7.2.6 Overall assessment

Additional simulations with fluid-structure interaction for model 2 were done for E equal to 0.8 MPa, 1.0 MPa, 2.0 MPa and 4.0 MPa. Corresponding plots for displacement and volume flow are included in appendix. Overall steady-state results for all simulation cases are also included in appendix, presented in table A.1.

Realistic trend lines representing how various values for Young's modulus affects the steady-state maximum velocity, the steady-state displacement of the epiglottic fold, and the steady-state volume flow at the outlet for the model 2 simulations are outlined and discussed in the following subsection.

Displacement

The steady-state values for displacement for each of the simulations are plotted against related values for Young's modulus, resulting in a steady-state displacement plot shown in figure 7.20.

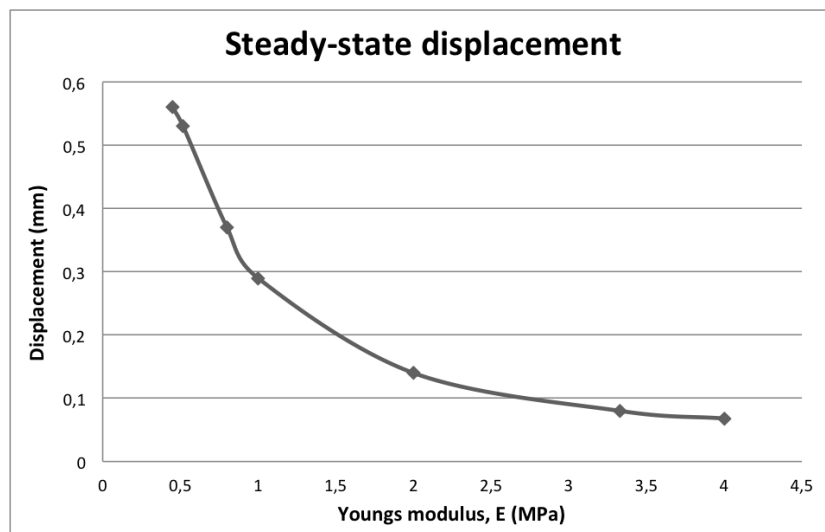


Figure 7.20: Steady-state displacement of the epiglottic fold as a function of Young's modulus.

The result clearly illustrates how the displacement of the solid part, i.e. the epiglottic fold, is reduced when the magnitude of Young's modulus increase. This implies that the epiglottic fold has its greatest displacement for low values of Young's modulus. The current findings are supported from the

definition of elasticity and modulus in section 5.3, namely that the greater value of Young's modulus, the harder is a deformation/displacement of the solid material, i.e. the epiglottic fold in this thesis.

Volume flow

A steady-state value for the volume flow at the outlet of the model is obtained for each of the various values for Young's modulus. The values are gathered in a steady-state volume flow plot, plotted against Young's modulus, and displayed in figure 7.21.

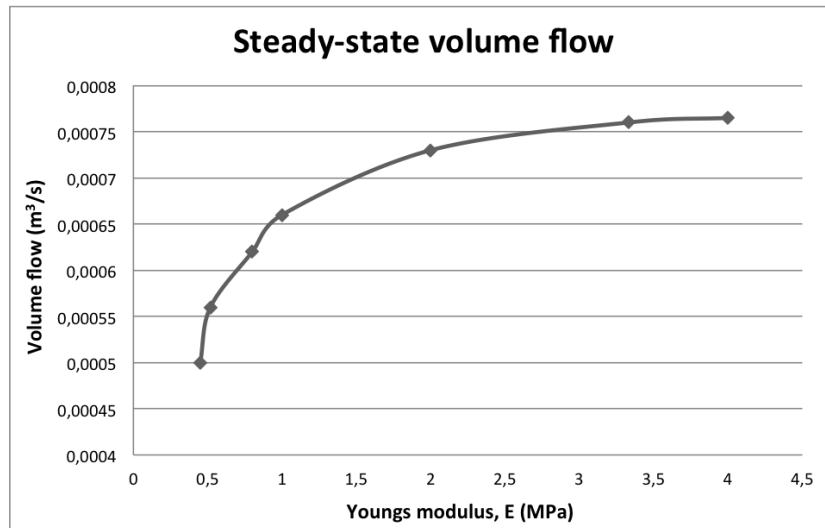


Figure 7.21: Steady-state volume flow at the outlet as a function of Young's modulus.

The result clearly shows how the value of the steady-state volume flow increases, i.e. the mass flow rate at the outlet increases, when the magnitude of Young's modulus increases. As the displacement increases with reduced magnitude of Young's modulus, it follows that the passage allowing air to pass freely is reduced. Hence the least amount of air reaching the outlet (representing the human lungs) is obtained for the smallest value of Young's modulus.

Velocity

The steady-state maximum velocity for each of the simulations are plotted against related values for Young's modulus, resulting in a steady-state maximum velocity plot illustrated in figure 7.22.

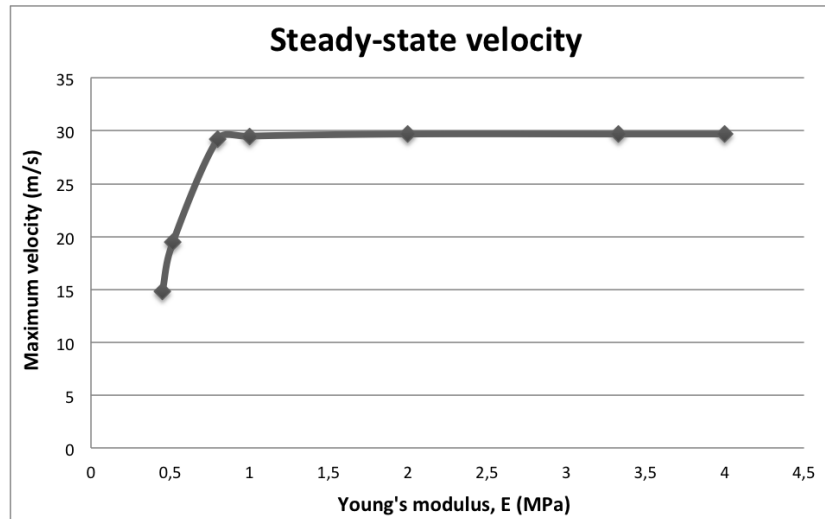


Figure 7.22: Steady-state maximum velocity obtained in the domain as a function of Young's modulus.

The result indicates that the steady-state maximum velocity in the domain increases as the magnitude of Young's modulus increases, until a value for Young's modulus equal to 0.8 MPa is reached. Above this value, the steady-state maximum velocity in the domain remains the same, i.e. 29.7 m/s. Based on the plot, a magnitude of Young's modulus equal to 0.8 MPa is suggested as a critical value for EILO patients. Hence, individuals having E smaller than 0.8 MPa can be suggested to qualify for the EILO diagnosis, based on the obtained velocity data.

7.2.7 Summary

The displacement plot suggests that a greater value of E reduces the displacement. Reduced displacement implies that the blockage of the fluid channel, i.e. the larynx, is significantly smaller. Consequently, with a smaller blockage, a larger amount of air is allowed to pass the obstacle. As the greatest value for volume flow at the outlet is obtained for such situations, it is reasonable that the greatest steady-state maximum velocity magnitude applies

for the greatest value of Young's modulus in accordance with the Bernoulli-equation, as the pressure drop is the driver of the flow.

Hence, a reduced value for Young's modulus will increase the displacement. Increased displacement implies greater blockage, which in turn causes a reduced maximum velocity in addition to a reduced volume flow at the outlet. The current findings/correlations are supported by Lacis [7] who suggested a decrease in volume flow rate for cases with a blocked larynx.

7.3 Real geometry with fluid structure interaction

As the geometry for model 3 is developed from CT images representing a real horse throat, more realistic simulations could possibly be obtained. Both a static and a dynamic situation was tried for model 3.0 and model 3.1, respectively.

Model 3.0

Firstly, a static simulation with an assigned constant inlet velocity equal to -0.5896 m/s, calculated in section 6.2 was run. Hence, the velocity at the inlet works as the driver of the fluid flow in model 3.0. The flow pattern for a real larynx without geometrical movement can be seen in figure 7.23.

The flow pattern indicates that the velocity increases as the cross-sectional area decreases. Hence, the highest velocity magnitude is observed in the narrowest part of the larynx, in accordance with literature for a situation driven by velocity.

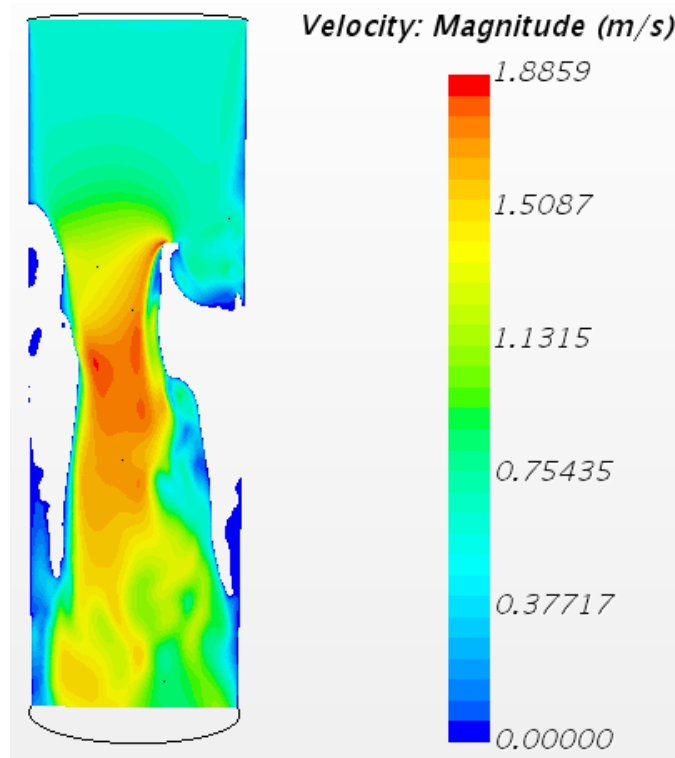


Figure 7.23: Flow pattern in a static larynx.

Model 3.1

To obtain a more realistic model for EILO in a horse, a dynamic simulation of a real geometry from CT images was attempted using fluid-structure interaction. As mentioned, the pressure drop works as the driver of the fluid flow in such situation. The inlet velocity for model 3.0 resulted in a corresponding pressure drop equal to -1.09 Pa, assigned as outlet boundary condition in the simulation for model 3.1.

The same simulation procedure as for model 2 was followed, with similar models and solvers chosen. Nevertheless, the simulation stopped running after two iterations, due to cells with negative values or with no volume.

Attempts were tried changing the boundary conditions, the base size of the computational grid and the magnitude of the time-step. Additionally, changing models and solvers were also tried. However, all the attempts ended with a floating point or a given number of cells without volume or with negative values in the cells. The balance between fluid forces and the structural

mechanics seems to be the major challenge in the programme.

Unfortunately, accomplishment of the planned work was therefore not possible during the time period of this thesis. Nevertheless, the process of solving the problem is continuously ongoing, and will proceed until a satisfactory solution to the problem is achieved and a functioning model is available.

7.3.1 Possibilities with a functioning model

Mylavarapu et al. [21] implied that proper numerical models of the human upper airway system could predict airway resistance and other crucial parameters, causing valuable input for surgeons in deciding the most appropriate surgery on a case-by-case basis. Several studies substantiates the suggestion of using numerical simulation models for patient-specific treatment optimization. De Backer [19] successfully predicted the outcome of treatment (with MAD) using an appropriate upper airway model in CFD. Göckan et al. [20] affirm the theory by the use of patient-specific models for evaluation of treatment planning. Additionally, experiments by Sul [23] indicates that proper computational models enables the study of air flow characteristics that could be difficult to achieve by experimental methods.

With these studies in mind, it is reasonable to assume that prediction of the actual situation occurring in a real throat during EILO can be predicted numerically. With a proper numerical model including fluid-structure interaction on a real geometry at hand, investigation of different physical parameters should be enabled. The effect of the physical changes should thereby be possible to predict. By varying the geometry and/or different variables, estimation of the most appropriate geometry and associated parameters will be possible. This will be of significant importance, both for the preparation of treatment, and especially for surgeons in their planning of a surgery. Knowledge of the impact of the various parameters in addition to increased understanding about the reinforcing factor may also be obtainable.

Additionally, there is an ongoing project by Z. Kelly from NMBU (Norwegian Environment and Bioscience University) where they try to measure the pressure drop in the larynx during a CLE-test. When pressure measurements are enabled, one can optimally implement the real laryngeal geometry into the simulation software, and assign appropriate values for pressure for each case. In such a way, the simulation will illustrate the exact situation arising in each specific case, with the right geometry and the associated pressure drop as input.

8 Concluding remarks

A numerical study of exercise-induced laryngeal obstruction was conducted using fluid-structure interaction. Properties like displacement, volume flow and velocity were investigated for various epiglottic fold positions, steered through a changing value for Young's modulus of the epiglottic fold. The objective was a better understanding of how the structural mechanics affect the fluid flow throughout a fluid-structure interaction in the throat. The numerical data were analyzed with an aim to identify why some individuals are affected by EILO while others are not.

The results show an increased displacement of the epiglottic fold when the value of Young's modulus decreases. Greater displacement of the epiglottic fold causes increased flow resistance in the domain, hence the amount of volume flow reaching the outlet decreases. A significant reduction (34 %) in volume flow at the outlet, i.e. the lungs, was observed when comparing an EILO value for Young's modulus of the epiglottic fold (E equal to 0.45 MPa) with a presumed normal larynx value for the epiglottic fold (E equal to 3.33 MPa). Thus, the results are in agreement with Lacis [7] who suggested a decrease in volume flow rate for cases with a blocked larynx.

The steady-state maximum velocity in the laryngeal domain is observed to increase with increasing magnitude of Young's modulus, until a value for Young's modulus equal to 0.8 MPa is reached. Hence, based on the obtained steady-state maximum velocity data, individuals having an epiglottic fold with E less than 0.8 MPa are suggested to qualify for the EILO diagnosis.

A decrease in the resistance of the solid part, as a function of physical time, was slightly indicated in some of the displacement plots. If such situation also applies for the epiglottic fold in a real geometry, it may indicate that the fold is subjected to fatigue, and thereby collapses easier. If so, it supports Gökcan et. al [20] suggestion that the aerodynamic properties in the larynx alter due to a loss in the muscular tonus. However, more research is needed to investigate the proposal.

All in all, the fluid-structure interaction method was successfully implemented in model 2, giving results in good correlation with literature. Therefore, it should be possible to implement this method into a more realistic geometrical model in future work, with numerous possibilities for further research.

9 Further work

Based on the work done in this thesis, there are many possibilities for further work with a functioning model available:

- **Fluid-structure interaction on simplified geometry with an experimentally measured pressure drop**

As there are ongoing studies trying to measure the pressure drop in a specific larynx before, during and after exercise, it will be reasonable to start out with a fluid-structure interaction on a simplified geometry (for instance model 2) with experimental results for pressure drop applied as boundary conditions.

- **Fluid-structure interaction on a real geometry from a horse and/or a human with corresponding pressure drop**

A reasonable continuation will be to carry out the started experiments tried in this thesis, namely fluid-structure interaction on a real geometry obtained from CT images of a horse with appropriate values for pressure drop for each individual case. The same applies for fluid-structure interaction of a human larynx with a corresponding pressure drop.

- **Investigate the influence of age on the physical properties in the throat**

Passman et al. [15] discovered an increase in modulus equal to 0.13 MPa per year age for a cricoid cartilage in horses. His research suggests that the characteristics of the cartilage will develop in line with the individual ageing. Assuming that this property also applies to a human cartilage, it may indicate why exercise induced laryngeal obstruction is most common among adolescents.

- **Experimentally investigate whether there are differences in Young's modulus for the epiglottic fold for humans**

In this thesis, various values for Young's modulus of the epiglottic fold were tested. However, there are no current experimental studies of this matter, so uncertainty are related to whether this is an issue that must be taken into account in the complex clinical picture.

- **Fatigue of the epiglottic fold**

Fatigue of the epiglottic fold was slightly indicated in some displacement plots in this study. However, further investigation, both experimentally and numerically, is necessary before the assertion can be confirmed or denied.

Nomenclature

Abbreviations

ALE	Arbitrary-Lagrangian-Eulerian
CFD	Computational Fluid Dynamics
CLE	Continuous Laryngoscopy Exercise
CT	Computed Tomography
EIA	Exercise Induced Asthma
EILO	Exercise Induced Laryngeal Obstruction
FSI	Fluid-Structure Interaction
FV	Finite Difference
FV	Finite Element
FV	Finite Volume
LES	Large Eddy Simulation
MRI	Magnetic Resonance Imaging
RANS	Reynolds-Averaged Navier-Stokes
SST	Shear Stress Transport
URF	Under-Relaxation Factor

Greek letters

α	dimensionless constant	
β	dimensionless constant	
ϵ	turbulence dissipation rate	$[\text{m}^2/\text{s}^3]$
κ	kinetic energy of turbulence	$[\text{m}^2/\text{s}^2]$

μ	dynamic viscosity	[kg/(m · s)]
ν	kinematic viscosity	[m ² /s]
ν_T	kinematic eddy viscosity	[m ² /s]
ω	specific turbulence dissipation rate	[s ⁻¹]
π	constant	[3.14]
ρ	density	[kg/m ³]
σ	stress	[N/m ²]
σ_k	dimensionless constant	
σ_ω	dimensionless constant	
τ_w	shear stress at pipe wall	[N/m ²]
ε	strain	

Nomenclature

\bar{u}	mean value velocity	[m/s]
A	area	[m ²]
a	acceleration	[m/s ²]
D	diameter	[m]
E	Young's modulus	[MPa]
F	force	[kg · m/s ²]
f	friction factor	
k	spring constant	[N/m]
l	point in undeformed body	[m]
l_o	point in deformed state	[m]

m	mass	[kg]
Ma	dimensionless mach number	
P	pressure	[Pa]
Q	volume flow	[l/min]
r	radius	[m]
Re	Reynolds number	
S	surface	[m ²]
t	time	[s]
u	velocity	[m/s]
u^+	dimensionless velocity quotient	
u^*	friction velocity	[m/s]
u'	deviating velocity	[m/s]
V	volume	[m ³]
v_E	minute ventilation	[l/min]
v_T	tidal volume	[m ³]
x	displacement	[m]
y^+	dimensionless distance	
z	depth	[m]

References

- [1] H. Opdahl, “Luftveisobstruksjon,” in *Store Norske Leksikon*, 2009.
- [2] “Hva er en luftveisobstruksjon?.” [Online] Available: <http://www.notmywar.com/hva-er-en-luftveisobstruksjon/>. Accessed: 2017-02-15.
- [3] C. S. Mehlum, E. S. Walsted, C. Godballe, and V. Backer, “Supraglottoplasty as treatment of exercise induced laryngeal obstruction (EILO),” *European Archives of Oto-Rhino-Laryngology*, pp. 945–951, Apr. 2016.
- [4] O. D. Røksund, J. H. Heimdal, J. Olofsson, R. C. Maat, and T. Halvorsen, “Larynx during exercise: the unexplored bottleneck of the airways,” *European Archives of Oto-Rhino-Laryngology*, pp. 2101–2109, Sept. 2015.
- [5] R. C. Maat, O. D. Røksund, J. Olofsson, T. Halvorsen, B. T. Skadberg, and J.-H. Heimdal, “Surgical treatment of exercise-induced laryngeal dysfunction,” *European Archives of Oto-Rhino-Laryngology*, pp. 401–407, Apr. 2007.
- [6] G. Mylavarapu, S. Murugappan, M. Mihaescu, M. Kalra, S. Khosla, and E. Gutmark, “Validation of computational fluid dynamics methodology used for human upper airway flow simulations,” *Journal of Biomechanics*, pp. 1553–1559, July 2009.
- [7] U. Lacis, *Modelling air flow in the larynx*. Master Thesis, Faculty of Science and Technology, Umeå University, 2012.
- [8] J. Tu, K. Inthavong, and G. Ahmadi, *Computational Fluid and Particle Dynamics in the Human Respiratory System*. Springer Science+Business Media Dordrecht, 2013.
- [9] “Testing Complete – for now.” [Online] Available: http://millysmuse.blogspot.com/2012/11/blog-post_20.html. Accessed: 2017-02-25.
- [10] “Thyroid cartilage larynx voice box hyoid bone laryngeal prominence adams apple.” [Online] Available: <http://vcgsb.info/thyroid-cartilage/thyroid-cartilage-larynx-voice-box-hyoid-bone-laryngeal-prominence-adams-apple-2/>. Accessed: 2017-05-16.
- [11] O. D. Røksund, R. C. Maat, J. H. Heimdal, J. Olofsson, B. T. Skadberg, and T. Halvorsen, “Exercise induced dyspnea in the young. Larynx as the bottleneck of the airways,” *Respiratory Medicine*, pp. 1911–1918, Dec. 2009.

- [12] H. E. Eckel, C. Sittel, P. Zorowka, and A. Jerke, “Dimensions of the laryngeal framework in adults,” *Surgical and Radiologic Anatomy*, pp. 31–36, Mar. 1994.
- [13] O. Trabelsi, A. P. del Palomar, J. L. López-Villalobos, A. Ginel, and M. Doblaré, “Experimental characterization and constitutive modeling of the mechanical behavior of the human trachea,” *Medical Engineering & Physics*, pp. 76–82, Jan. 2010.
- [14] D. Shinwari, R. C. Scherer, K. J. DeWitt, and A. A. Afjeh, “Flow visualization and pressure distributions in a model of the glottis with a symmetric and oblique divergent angle of 10 degrees,” *The Journal of the Acoustical Society of America*, pp. 487–497, Jan. 2003.
- [15] S. N. Passman, J. Cheetham, L. J. Bonassar, N. G. Ducharme, and J. J. Rawlinson, “Biomechanical characterisation of equine laryngeal cartilage,” *Equine Veterinary Journal*, pp. 592–598, Sept. 2011.
- [16] M. d. Vries, H. Schutte, A. Veldman, and G. Verkerke, *Glottal flow through a two-mass model: Comparison of Navier-Stokes solutions with simplified models*. PhD thesis, University Medical Center Groningen, University of Groningen, 2002.
- [17] M. K. Gökcan, E. Günaydinoglu, and D. F. Kurtuluş, “Effect of glottic geometry on breathing: three-dimensional unsteady numerical simulation of respiration in a case with congenital glottic web,” *European Archives of Oto-Rhino-Laryngology*, pp. 3219–3229, Oct. 2016.
- [18] A. Hundertmark-Zaušková, R. Lehmann, M. Hess, and F. Müller, “Numerical simulation of glottal flow,” *Computers in Biology and Medicine*, pp. 2177–2185, Dec. 2013.
- [19] J. W. De Backer, O. M. Vanderveken, W. G. Vos, A. Devolder, S. L. Verhulst, and V. et al., “Functional imaging using computational fluid dynamics to predict treatment success of mandibular advancement devices in sleep-disordered breathing,” *Journal of Biomechanics*, pp. 3708–3714, 2007.
- [20] M. K. Gökcan, D. F. Kurtuluş, E. Üstüner, E. Özyürek, G. G. Kesici, Erdem, G. Dursun, and C. Yağci, “A computational study on the characteristics of airflow in bilateral abductor vocal fold immobility,” *The Laryngoscope*, pp. 1808–1818, Sept. 2010.

- [21] G. Mylavarapu, M. Mihaescu, L. Fuchs, G. Papatziarnos, and E. Gutmark, “Planning human upper airway surgery using computational fluid dynamics,” *Journal of Biomechanics*, pp. 1979–1986, Aug. 2013.
- [22] M. Mihaescu, S. Khosla, S. Murugappan, and E. Gutmark, “Unsteady laryngeal airflow simulations of the intra-glottal vortical structures,” *The Journal of the Acoustical Society of America*, pp. 435–444, Jan. 2010.
- [23] B. Sul, A. Wallqvist, M. J. Morris, J. Reifman, and V. Rakesh, “A computational study of the respiratory airflow characteristics in normal and obstructed human airways,” *Computers in Biology and Medicine*, pp. 130–143, Sept. 2014.
- [24] V. Rakesh, A. K. Datta, N. G. Ducharme, and A. P. Pease, “Simulation of turbulent airflow using a CT based upper airway model of a racehorse,” *Journal of Biomechanical Engineering*, June 2008.
- [25] X. Liu, W. Yan, Y. Liu, Y. S. Choy, and Y. Wei, “Numerical Investigation of Flow Characteristics in the Obstructed Realistic Human Upper Airway,” *Computational and Mathematical Methods in Medicine*, Sept. 2016.
- [26] S. Li, R. C. Scherer, M. Wan, S. Wang, and H. Wu, “The effect of glottal angle on intraglottal pressure,” *The Journal of the Acoustical Society of America*, pp. 539–548, Jan. 2006.
- [27] J. D. Anderson, *Computational Fluid Dynamics: The Basics with Applications*. McGraw-Hill series in mechanical engineering, New York: McGraw-Hill, 8. ed., 1995.
- [28] W. L. McCabe, J. C. Smith, and P. Harriott, *Unit Operations of Chemical Engineering*. Boston, Mass.: McGraw-Hill Higher Education, 7. ed., 2005.
- [29] “Introduction to finite difference method and fundamentals of cfd.” [Online] Available: <http://nptel.ac.in/courses/112104030/lecture1/1.8.htm>. Accessed: 2017-05-20.
- [30] “Methodology.” [Online] Available: http://www.kostic.niu.edu/340/_340-Posted/STAR-help/method/star_method.pdf, 2005. Accessed: 2017-02-14.
- [31] CD-adapco, *User Guide Star-CCM+ 10.06*. Siemens PLM Software, 2015.

- [32] J. Warnatz, U. Maas, and R. W. Dibble, *Combustion: physical and chemical fundamentals, modeling and simulation, experiments, pollutant formation*. Springer, 2006.
- [33] A. L. Bloxom, *Numerical Simulation of the Fluid-Structure Interaction of a Surface Effect Ship Bow Seal*. Doctoral Thesis, University of Blacksburg, Blacksburg, VA, Dec. 2014.
- [34] E. H. Herø, *Programming turbulence models in FORTRAN*. Master Thesis, Department of Energy and Process Engineering, Norwegian University of Science and Technology, June 2015.
- [35] “SST k-omega model.” [Online] Available: https://www.cfd-online.com/Wiki/SST_k-omega_model. Accessed: 2017-02-07.
- [36] M. Larsson and B. Müller, *Numerical Modeling of Fluid-Structure Interaction in the Human Larynx*. Doctoral Thesis, Norwegian University of Science and Technology, Department of Energy and Process Engineering, Nov. 2010.
- [37] E. Lefrancois and J. P. Boufflet, *An Introduction to Fluid-Structure Interaction: Application to the Piston Problem**. Doctoral Thesis, Université de Technologie de Compiègne, Roberval, France, 2010.
- [38] J. R. Lien and G. Løvholden, *Generell fysikk for universitet og høyskoler: Bind 1 mekanikk*. Universitetsforlaget, 2010.
- [39] P. A. Yushkevich, G. Gerig, and Y. Gao, “itk-SNAP.” [Online] Available: <http://www.itksnap.org/pmwiki/pmwiki.php?n=Main.Credits>, 2011.
- [40] “Regulation of Ventilation During Exercise | Exercise Physiology.” [Online] Available: <http://ptexphys.utorontoeit.com/respiratory-physiology/regulation-of-ventilation-during-exercise/>. Accessed: 2017-02-13.
- [41] “Lung volumes.” [Online] Available: https://en.wikipedia.org/w/index.php?title=Lung_volumes&oldid=764757577. Accessed: 2017-02-15.

A Additional results for model 2

Additional plots for displacement of the epiglottic fold and volume flow at the outlet is added in the following appendix. The steady-state values from the plots are already included in the unified plots in figure 7.20 and figure 7.21.

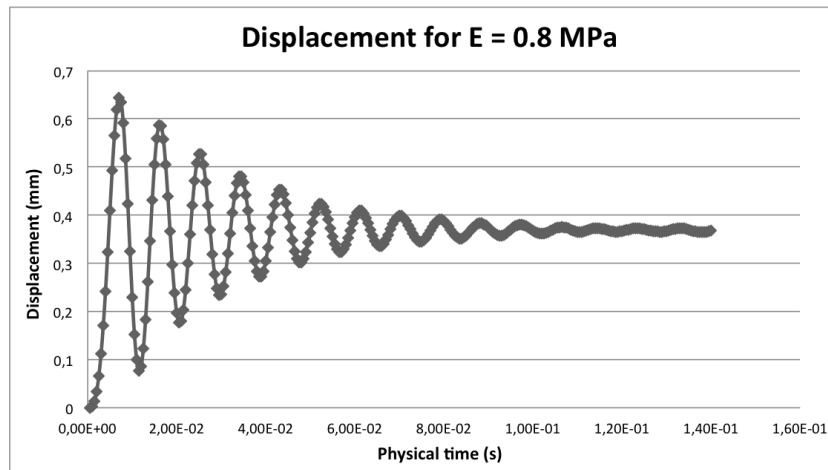


Figure A.1: Displacement for $E = 0.8$ MPa. The solid part has a maximum displacement equal to 0.64 mm, and becomes steady at 0.37 mm.

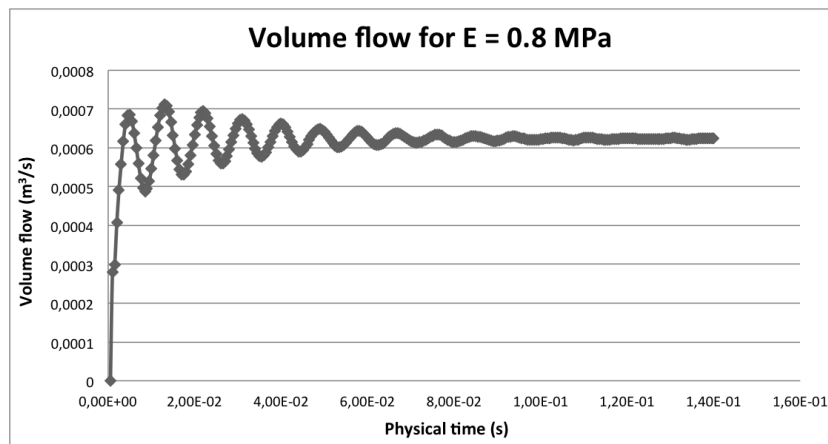


Figure A.2: Volume flow at the outlet for $E = 0.8$ MPa. A minimum flow equal to 0.000488 m^3/s is reached, and the flow becomes steady at 0.00062 m^3/s .

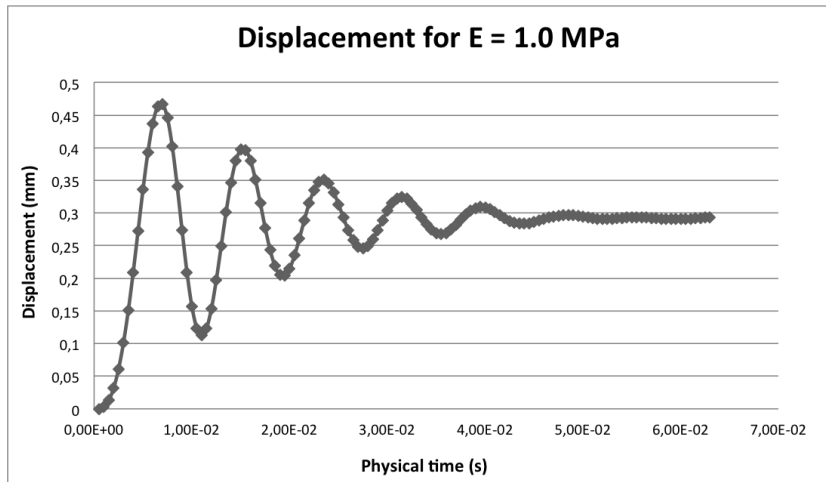


Figure A.3: Displacement for $E = 1.0$ MPa. The solid part has a maximum displacement equal to 0.46 mm, and becomes steady at 0.29 mm.

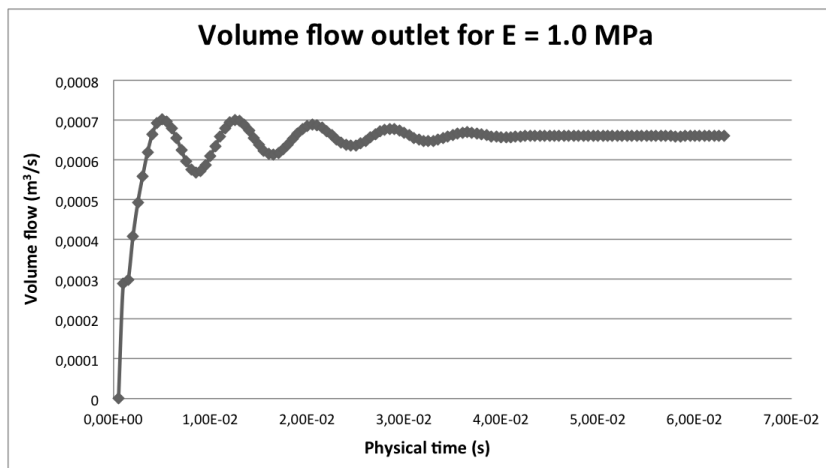


Figure A.4: Volume flow at the outlet for $E = 3.33$ MPa. A minimum flow equal to 0.00056 m^3/s is reached, and the flow becomes steady at 0.00066 m^3/s .

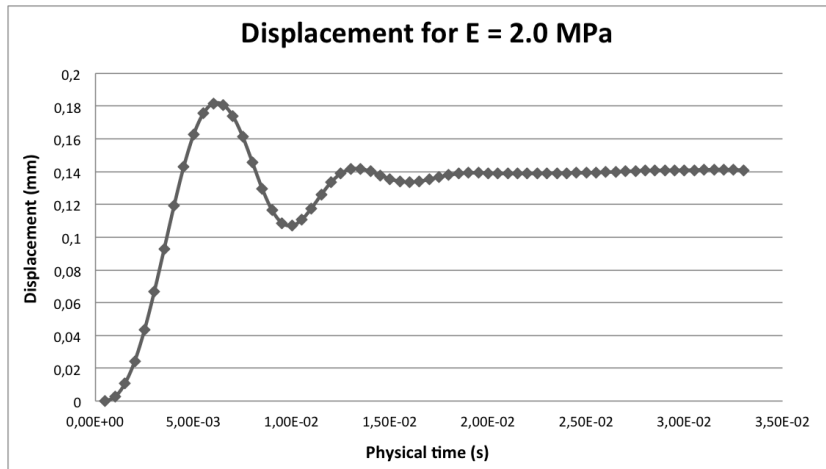


Figure A.5: Displacement for $E = 2.0$ MPa. The solid part has a maximum displacement equal to 0.18 mm, and becomes steady at 0.14 mm.

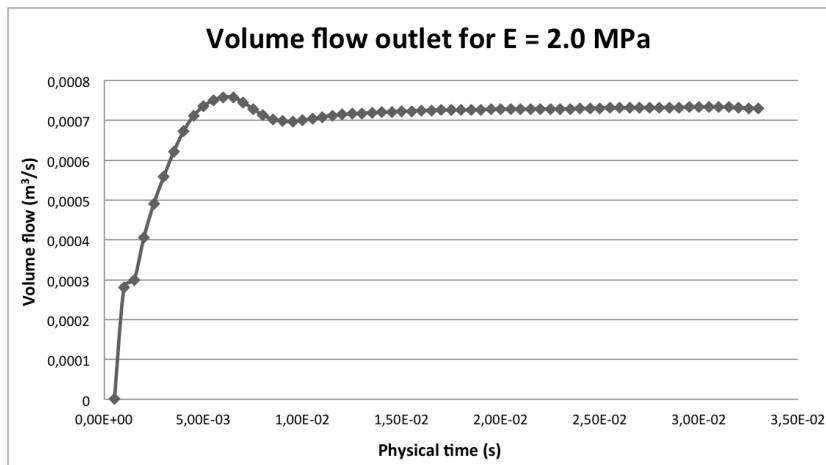


Figure A.6: Volume flow at the outlet for $E = 3.33$ MPa. A minimum flow equal to 0.000698 m^3/s is reached, and the flow becomes steady at 0.00073 m^3/s .

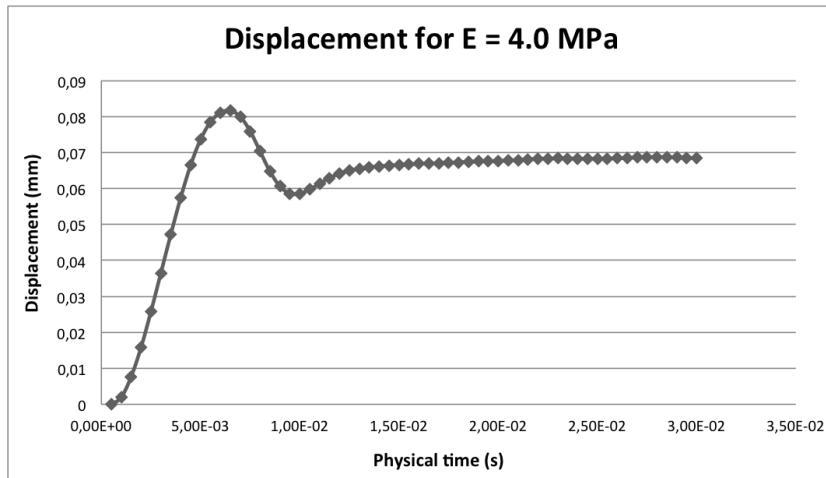


Figure A.7: Displacement for $E = 4.0$ MPa. The solid part has a maximum displacement equal to 0.08 mm, and becomes steady at 0.068 mm.

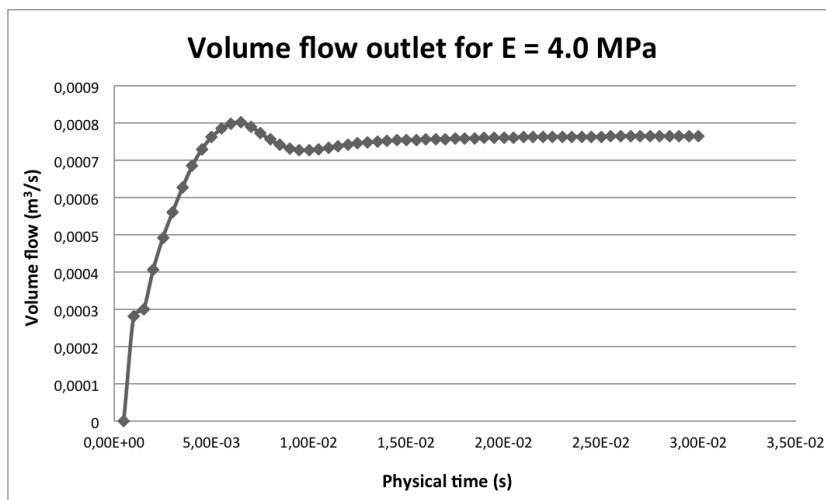


Figure A.8: Volume flow at the outlet for $E = 3.33$ MPa. A minimum flow equal to 0.000727 m³/s is reached, and the flow becomes steady at 0.000765 m³/s.

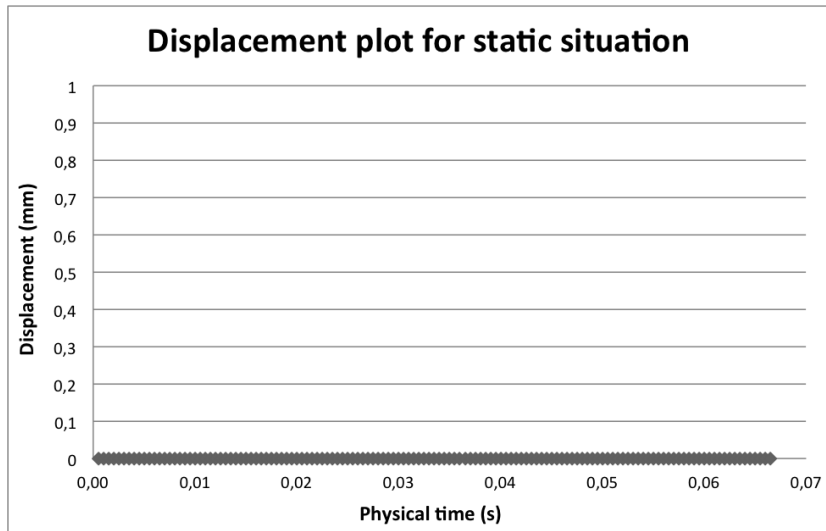


Figure A.9: Static displacement plot for model 2. As expected, there are no displacement of the epiglottic fold for the static simulation.

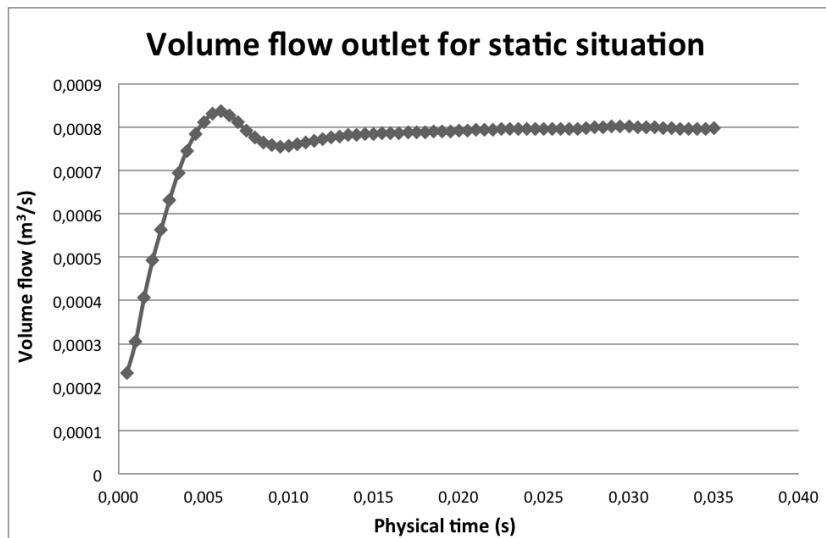


Figure A.10: Volume flow at the outlet for a static situation in model 2. The flow becomes steady at $0.0008 \text{ m}^3/\text{s}$.

Figure A.11 displays the velocity development in the domain for the static situation, i.e. no movement of the epiglottic fold.

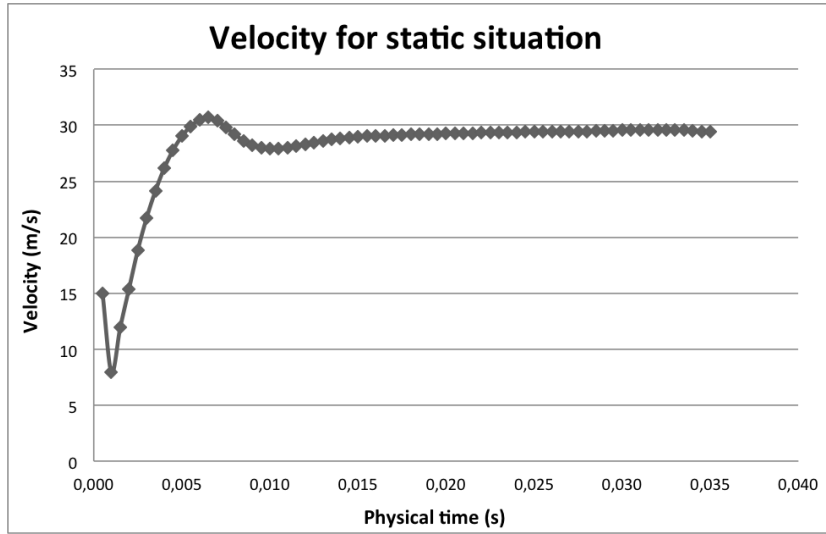


Figure A.11: Velocity plot for static situation. Steady-state maximum velocity equal to 29.6 m/s is obtained.

The overall result for all the eight different simulation cases are presented in table A.1.

Table A.1: Overall values for steady-state displacement, steady-state minimum volume flow at the outlet and steady-state maximum velocity for various values of Young’s modulus.

E (MPa)	Displacement (mm)	Volume flow (m ³ /s)	Velocity (m/s)
0.45	0.56	0.0005	14.8
0.518	0.53	0.00056	19.5
0.8	0.37	0.00062	29.2
1.0	0.29	0.00066	29.5
2.0	0.14	0.00073	29.7
3.33	0.08	0.00076	29.7
4.0	0.068	0.000765	29.7
Static	0	0.0008	29.7

Figure A.12 illustrates the velocity development as a function of physical time for various values of Young's modulus.

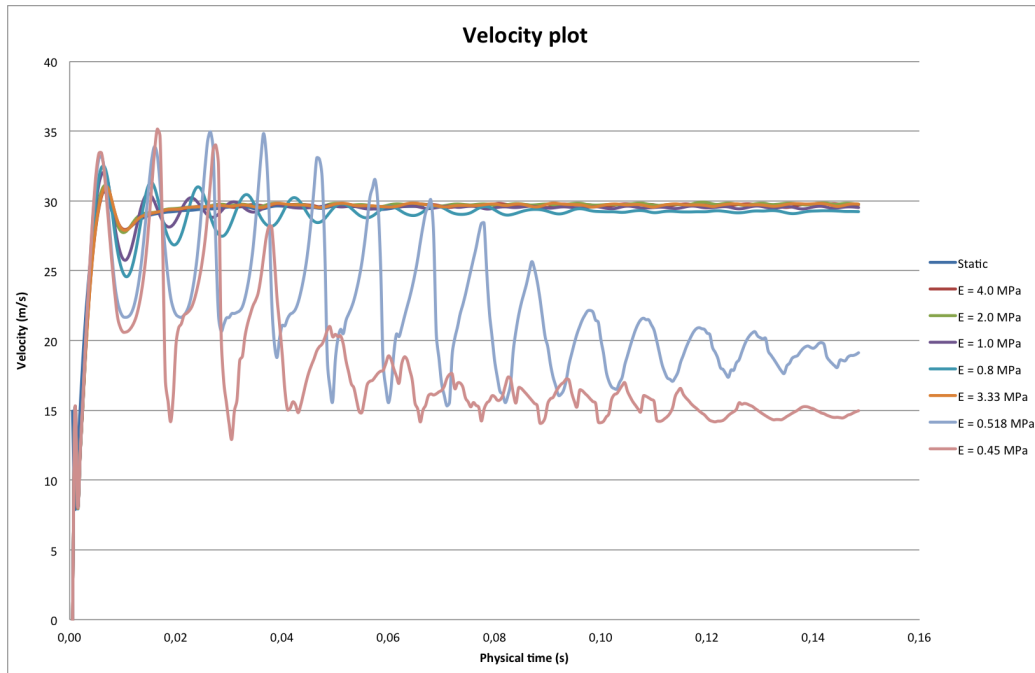


Figure A.12: Velocity plot for various values of Young's modulus.